Materials & Design 207 (2021) 109858

Contents lists available at ScienceDirect

Materials & Design

journal homepage: www.elsevier.com/locate/matdes

The effect of build direction and geometric optimization in laser powder bed fusion of Inconel 718 structures with internal channels

Galina Kasperovich [a,*], Ralf Becker [b], Katia Artzt [a], Pere Barriobero-Vila [a], Guillermo Requena [a,c], Jan Haubrich [a]

[a] Institute of Materials Research, German Aerospace Center (DLR), Linder Hoehe, D-51147 Cologne, Germany
[b] Institute of Propulsion Technology, German Aerospace Center (DLR), Linder Hoehe, D-51147 Cologne, Germany
[c] RWTH Aachen University, Metallic Structures and Materials Systems for Aerospace Engineering, D-52062 Aachen, Germany

HIGHLIGHTS

- Significant improvement in dimensional accuracy of Inconel 718 thin channels produced by laser powder fusion (LPBF) through a multi-component optimization is achieved.
- Roughness of flat surfaces tilted at 0°, 45°, 90° and 135° to the working platform is optimized.
- Build direction effect on the quality of inclined shaped channels is analysed using computed tomography.
- Optimized LPBF contour parameters in combination with modified channel shapes allowed nearly ideally round channels in all building orientations for design of combustion chambers for future aircraft engines.

GRAPHICAL ABSTRACT

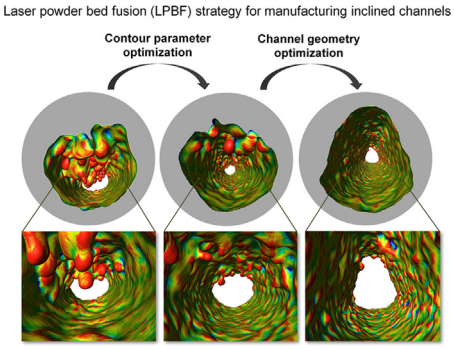

ARTICLE INFO

Article history:
Received 25 February 2021
Revised 20 May 2021
Accepted 30 May 2021
Available online 1 June 2021

Keywords:
Inconel 718
Laser powder bed fusion
Selective laser melting
Computed tomography
Surface roughness
Channel structures

ABSTRACT

A laser powder bed fusion (LPBF) strategy was developed for manufacturing small channels with high dimensional accuracy in Inconel 718 structures. Particular attention was paid to surface characteristics such as equivalent diameter and shape factor. The inherent surface quality of external surfaces was optimized by a systematic variation of the LPBF contour parameters as well as the channel cross-section. The mean arithmetic roughness S_a was analysed for upskin, vertical and downskin surfaces with respect to the build platform. Simultaneously, the effect of the build direction on the quality of internal free-shaped surfaces was investigated on channels with diameters from 500 to 1000 μm and build orientations from the horizontal (0°) to vertical (90°). A significant improvement in dimensional accuracy was achieved by using an optimized droplet-shaped cross-section that is scaled as a function with the build inclination. An angular analysis of the surface roughness in different regions of the channels confirms that this modified cross-section reduces the fraction of channel regions that show a particularly high surface roughness due to inward melting. In combination with an optimized contour processing strategy, the modified channel resulted in the best properties for inclinations below 45°. The shape factor increased from 0.4 to almost 0.9, i.e., close to the ideally round shape.

* Corresponding author.
E-mail address: galina.kasperovich@dlr.de (G. Kasperovich).

https://doi.org/10.1016/j.matdes.2021.109858
0264-1275/

1. Introduction

Laser powder bed fusion (LPBF) is one of the preferred additive manufacturing (AM) technologies for creating highly complex metallic components directly from digital models by melting metal powders layer-by-layer [1–3]. Geometrically demanding components with integrated functional features such as precisely placed cooling channels that are often very difficult, expensive or sometimes even impossible to manufacture with conventional manufacturing technologies can be produced by LPBF [4–6].

Processing Nickel-based alloys and, in particular, Inconel 718 (IN718) by LPBF has received a lot of attention in the last years [7,8]. Inconel 718 is characterized by a high strength, good fatigue properties as well as oxidation and corrosion resistance at elevated temperatures of up to 700 °C [9,10]. For these reasons, conventionally manufactured IN718 is widely used for high temperature applications in aerospace industry, gas turbines, turbocharger rotors, nuclear reactors, highly-loaded rotating parts, and a variety of other applications [11–13]. For example, IN718 is of interest for use in aircraft engine components such as combustion chambers with a modern cooling system consisting of multiple thin internal channels [14–18]. For the latter applications, the surface roughness and dimensional tolerance of internal channels are critical. Along with the powder deposits on the walls, the roughness adversely affects the functionality of the cooling systems and leads to a decrease in the flow rate due to high friction, possible turbulence, loss of pressure and loose particles that could damage other equipment.

However, LPBF has certain drawbacks that require further investigations and optimizing the processing parameters and strategies for specific geometries and components. LPBF generally leads to poor surface qualities caused by the staircase effect on both upward- and downward-facing surfaces (i.e., due to discrete layer thicknesses in generative processes) as well as coarse melt tracks and adhering, incompletely molten powder particles [19]. The effect of the process parameters on the final part quality or on related mechanical properties has been investigated in many works for a variety of alloys. Fox et al. [20] researched the relationship between surface roughness, laser power, scan speed, and overhang angles in LPBF of stainless steel, reporting that the surfaces are dominated by partially molten powder particles and material from re-solidified melt tracks. Especially downskin surfaces show very high roughness [20,21]. The influence of the build angle on the produced surfaces is hard to tackle since the design of the part itself can generally not be changed readily [22]. Moreover, support structures may be needed on some part areas [23,24], which leads to additional manufacturing steps due to support removal and surface post-processing requirements. This can also result in defects such as ridge formation, causing an even higher surface roughness [25,26]. Several studies of LPBF surface qualities have been motivated by the possibility of reducing residual stresses [27–29].

Using processing parameters for the contour region that differ from volume parameters can strongly improve the surface smoothness [20,28–31]. In particular, the surface qualities of the widely-used titanium alloy Ti–6Al–4 V produced with different LPBF parameters have been studied in depth in several works (see, e.g., Refs. [32–35]). Fewer works are available on the influence and optimization of the LPBF process on the surface quality for the family of Ni-based alloys. The roughness for Inconel 625 specimens has been minimized by parameter optimization by Mumtaz and Hopkinson [36]. They performed a full factorial analysis of the top and side surface roughness of thin-wall parts and found that parameter changes tending to decrease roughness on one surface increase it on the other. Since roughness is often not only an aesthetic issue but can also lead to crack nucleation, it is directly linked with fatigue life. This was studied, for example, for Inconel 625 [37] and Inconel 718 [38]. Whip et al. [39] investigated the relationship between contour process parameters and surface roughness for LPBF Inconel 718 using both non-destructive and destructive measurement techniques and showed that an understanding of surface roughness can be used to further process optimization and to justify the qualification strategy for AM components. Caiazzo et al. [40] studied the effect of volumetric energy density on the surface roughness of LPBF Inconel 718 and statistically analysed it in terms of optimality between internal porosity of the parts and the quality of their top surface.

Several methods exist for improving surface quality through mechanical and chemical post-processing treatments, but these generally depend on the part geometry. Baicheng et al. [41], for instance, showed significant reduction in the roughness of the external LPBF IN718 surfaces using electrochemical polishing methods. However, the final quality of LPBF parts with complex internal surfaces is difficult to improve due to a lack of suitable post-processing routes, requiring the surface qualities to be improved rather through the use of optimized LPBF contour parameters. Despite a few studies completed in this direction [42–46], there is still a long way to go towards an accurate understanding of the influence of the process parameters on the resulting surface characteristics [19].

Numerous standard techniques are being used today for measuring surface roughness, but most are inept at characterizing the internal surfaces in freeform geometries. Non-destructive methods such as X-ray computed tomography (CT) significantly expand the ability to analyse geometric accuracy. Stimson et al. [15,16] and Snyder et al. [17] investigated CoCr and Inconel 718 coupons with internal channels fabricated by AM (i.e., laser-based directed energy deposition (DED) in this case) for different build directions with CT. Cylindrical channels were built in three different orientations, while teardrop and diamond channels were built horizontally. After analysis of internal surface roughness and dimensionality from CT, the heat flux was tested on an experimental facility, allowing a correlation between surface roughness, friction factor and heat flux. Moreover, Klingaa et al. [18] investigated channels with a diameter of 2 mm produced at different inclinations by LPBF in 17–4 PH stainless steel. They extracted local and radial roughness profiles from CT data and calculated the roughness values in the channels by means of a simple regression model.

The goal of the present study is to investigate the effects of the processing strategy and the build direction on the quality of small internal channels in Inconel 718 structures produced by LPBF and to improve their geometrical accuracy by a combination of manufacturing parameters, scan strategy and geometrical shape optimization. First, the roughness of flat external surfaces inclined at the angles of 0°, 45°, 90° and 135° with respect to the working platform was minimized through a variation of the LPBF contour parameters. Secondly, internal channels integrated in cylinders were investigated to evaluate the effect of the build direction on the quality of internal channels with the diameters of 500, 700 and 1000 μm inclined at 0°, 22.5°, 45° and 90 by means of X-ray computed tomography. The quantitative results were used to round- and adapt droplet-shaped channels for special test elements with channels of 1000 μm target diameter as a function of the build direction in the third investigation stage. Using optimized LPBF contour parameters in combination with the modified channel shapes allowed manufacturing geometrically accurate, nearly ideally round channels in all building orientations suitable for the design of combustion chambers for future aircraft engines.

Table 1
Nominal composition of the IN718 alloy powder (wt.%).

Ni	Cr	Fe	Nb	Mo	Ti	Al	Co	Mn	C
Bal.	18.70	18.49	5.30	2.93	0.95	0.42	0.03	0.07	0.042

2. Experimental methods

2.1. Sample manufacturing using LPBF

Inconel 718 alloy powder, provided by AP&C (Boisbriand, Canada), was produced by plasma atomization in a high purity argon atmosphere, resulting in mostly spherical particles. The particle size distribution, measured by a particle size analyser (LS 13320 PIDS, Beckman Coulter, Krefeld, Germany), has D-values of 22 μm (D10), 33 μm (D50) and 45 μm (D90). The nominal chemical composition of the IN718 powers determined by means of X-ray fluorescence analysis (RFA) by RevierLabor© (Essen, Germany) is given in a Table 1. The powder complies with the regulation AMS5662 [47].

A Concept Laser M2 machine (Concept Laser GmbH, Lichtenfels, Germany) equipped with a 200 W diode-pumped ytterbium fibre laser, operating in continuous wave-mode with a Gaussian beam shape, was used to manufacture the LPBF specimens. The laser power, scanning speed and hatch distance for the samples' bulk were first optimized in terms of minimum porosity (<0.3%) at a high build-up rate of 10.6 cm^3/h. The resulting volumetric energy density E_V, which is usually described as the ratio between laser power P, scanning speed v, hatch distance h and layer thickness t as $E_V = P/(v \times h \times t)$, was kept constant at 60 J/mm^3 for all samples build at a layer thickness of t = 30 μm.

Three types of samples were produced for the three stages of this study.

2.1.1. Samples with external flat surfaces for roughness optimization

The sample geometry shown in Fig. 1 (a) was used to investigate the general influence of the contour parameters on surface roughness. In total, two build jobs with 49 samples in each batch were produced for the analysis of different contour scan parameters, scan strategies and the build platform positioning (Fig. 1 (b)). The three side surfaces of the specimens oriented at 45°, 90° and 135° with respect to the working platform were analysed. In this case, the 45° surface corresponds to the reverse side of the 135°. Upskin (45°), inskin (90°) and downskin (135°) are the main types of surfaces that possess roughnesses much higher than upward-facing surfaces (0°). The latter are not considered in this study.

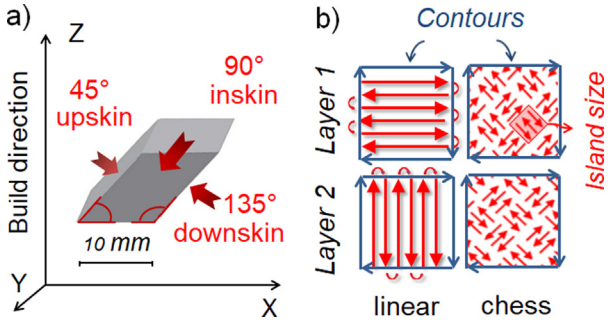

Fig. 1. (a) Sketch of the samples produced to study roughness. (b) Volumetric hatching strategies: linear strategy (red arrows) with a rotation of 90° between adjacent layers and chess hatching within small square islands. Blue arrows in (b) represent contours produced separately. (For interpretation of the references to colour in this figure legend, the reader is referred to the web version of this article.)

The energy descriptor used for the contour parameter sets is the linear energy density $E_L = P_{CL}/v_{CL}$, i.e. the ratio between laser power P_{CL} and scanning speed v_{CL}.

Two main scan strategies, i.e. with linear and checkerboard patterns (Fig. 1 (c)), were chosen for volume hatching. Linear is a hatching technique using parallel scan vectors in alternating directions, which are rotated by 90° between adjacent layers. Chess (or checkerboard) is a small square island-based strategy as recommended for reducing the effect of residual stresses [28,29]. A 5 × 5 mm^2 island size was used, which was also rotated by 90° from layer to layer. The reason for rotating the islands is that the vectors are not always on the same place and the start and end points are also staggered.

Four studies were carried out to optimize the LPBF parameters to achieve low surface roughness:

- an analysis of sample location on the build platform to assess positioning effects and reproducibility
- a simultaneous variation of the contour laser power P_{CL} and the contour scan speed v_{CL} while keeping constant linear energy density E_L = 0.113 J/mm (P_{CL}-v_{CL} variation)
- a variation study of the scan strategy of the contour vectors (contour vector scan sequence)
- a linear energy density E_L variation with unconstrained scan speed v_{CL} at constant P_{CL}.

The investigated combinations of contour parameters, scan strategies and sample positions are given in Table 2.

2.1.2. Cylindrical samples with internal channels for the study of build direction related effects

The influence of the build orientation on the continuity, diameter and surface quality of the internal channels was examined on cylinders manufactured at angles of 0°, 22.5°, 45° and 90° with respect to the building platform. All samples were analysed by CT (see Section 2.3). Each cylinder with an outer diameter of 5 mm and a length of 20 mm (Fig. 2 (a)) had 3 sets of 3 identical internal channels parallel to the cylinder axis with given target diameters of 500 μm, 700 μm and 1000 μm. Two basic shapes were investigated with the goal to obtain an ideally round shape of the channels from LPBF: round in each build direction (Fig. 2 (b)) and droplet-shaped cross sections at angles of 0° and 22.5° (s. **Fig. S1** (a-j) in **supplementary materials**). The geometry of the initially tested droplet channels used in these specimens consists of a circle with triangular extension with a small upper rounding of 25 μm presented in **Fig. S3 (b)** and **Table S1** in **supplementary materials.**

In the case of droplet channels, the target diameter also varied between 500 μm, 700 μm, and 1000 μm, but the actual equivalent diameter considering the elongated upper part given by the CAD model was greater, namely 522 μm, 731 μm, and 1044 μm (Fig. 2 (c)). Fig. 2 (d) shows a droplet-shaped geometry in channels inclined at 0° and 22.5°.

The effects of build direction on the quality of internal shaped surfaces was investigated in parallel with the optimisation of the roughness of the external flat surfaces, according to Section 2.1.1. Since the optimised contour parameters were not yet known, all cylinders were fabricated with the constant reference parameters based on machine settings: E_L = 0.113 J/mm: P_{CL} = 180 W and

Table 2
Contour parameter optimization (at constant volumetric energy density E_v for bulk processing of 60 J/mm^3 using the bulk hatching and LPBF parameters given in Section 2.1). P_{CL} and v_{CL} indicate the laser powder and scan speed of the parameters used for the contour lines.

Contour variations	Platform position	Laser power P_{CL} [W]	Scan speed v_{CL} [mm/s]	Line energy density E_L [J/mm]	Scan strategy
1. Platform positioning analysis	top left top right centre bottom left bottom right	180	1600	0.113	inside → outside
2. P_{CL}-v_{CL} Variation (E_L = const.)	centre	67.5	600	0.113	inside → outside
		90.0	800		
		112.5	1000		
		135.0	1200		
		157.5	1400		
		180.0	1600		
		199.7	1775		
3. Contour vector scan sequence	centre	180	1600	0.113	inside → outside inside → 2 × outside outside → inside → outside 2 × outside → inside → outside 2 × outside → inside
4. Energy density variation ($E_L \neq$ const) at $v_{CL} \neq$ const	centre	180	600	0.300	inside → outside
			800	0.225	
			1000	0.180	
			1100	0.164	
			1600	0.113	
			2000	0.090	
			2100	0.086	

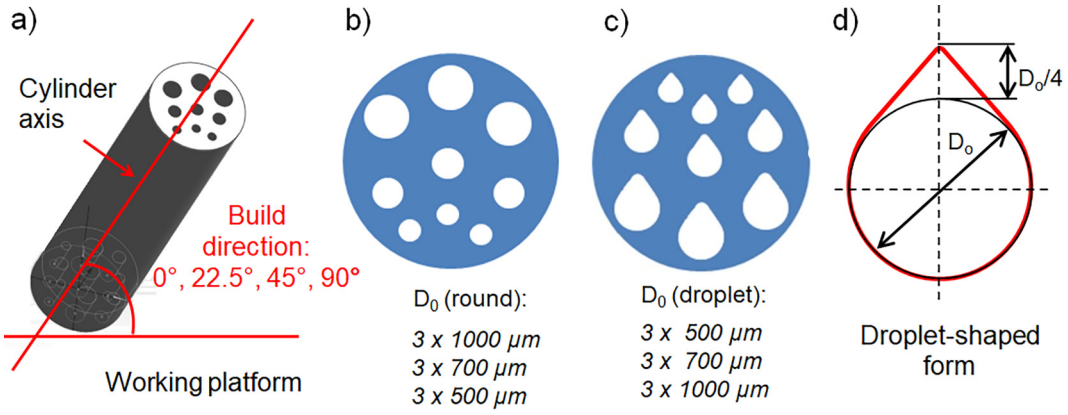

Fig. 2. Cylindrical samples used for the study of the build direction effects: (a) CAD model showing the build direction to the working platform with 9 internal channels: (b) round- and (c) droplet-shaped. (d) Droplet-shaped geometry in channels inclined at 0° and 22.5°.

v_{CL} = 1600 mm/s. A single contour line at the chess bulk strategy was used.

2.1.3. Test segments with internal channels

For further development of a strategy to manufacture cooling elements for new combustion chamber designs in aircraft engines, the contour parameters optimized in the first stage of the study were transferred to rectangular wall elements with variable channel geometries, considering the build-angle effects from the second stage. The elements have a cross section of 4 × 7 mm^2 and a length of 10 mm (Fig. 3 (a)) and incorporate longitudinal channels of different shapes: round and droplet-shaped ones. The target diameter for channels was 1000 µm. In combustion chambers the channels can be placed at build angles below 45°. Thus, inclinations of 45° and 22.5° with respect to the build platform were chosen as well (Fig. 3 (b) from top to bottom, respectively). Fig. 3 (c) shows a modified droplet-shaped geometry used in the final test elements.

While investigating the influence of the build direction in the cylindrical samples (Sections 2.1.2), a reduction of height of the round channels roughly proportional to the cosine of the inclination was found (see Section 3.3 and **Fig. S2**, **supplementary materials**). Therefore, the droplet-shaped channels were modified in the final test segments by replacing the triangular extension by a second circle scaled with the cosine of inclination. This smaller circle was connected by tangential lines to the main channel, providing an optimized droplet shape (see **Fig. S3 (c)** and **Table S1**, **supplementary materials**). The actual equivalent diameter of the droplet channels, considering the elongated top increased to 1148 µm and 1044 µm for build angles of 22.5° and 45°, respectively.

Different horizontal positions of these test elements on the working platform (in plane: XY = 10°, 40°, 70° and 100° with respect to the build direction Z as shown in Fig. 3 (b)) were investigated, whereby potential effects due to the location and orientation were studied.

Volumetric parts were produced with E_V = 60 J/mm^3 (i.e. with optimized volumetric parameters as given in Section 2.1). The values obtained as the result of the optimization in the first stage of this study were used as final contour scan parameters, namely

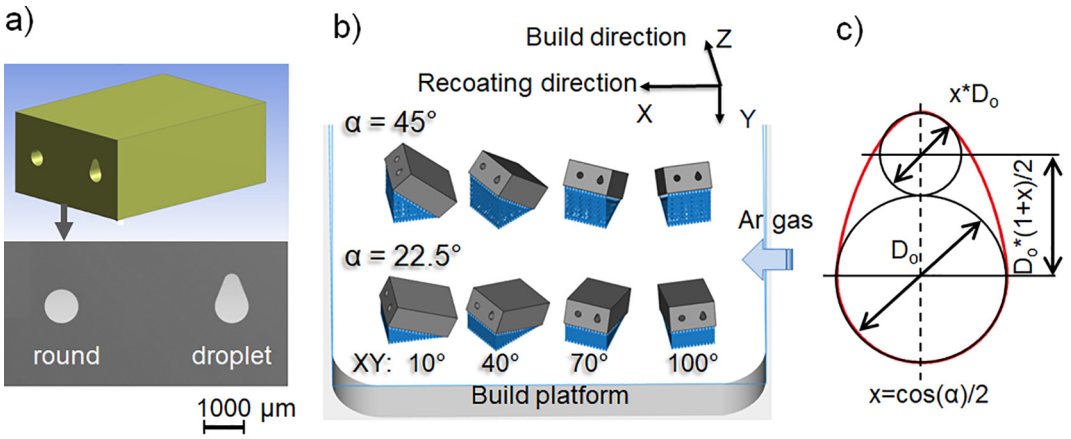

Fig. 3. Final test elements 10 × 4 × 7 mm³ for the optimization of the channel structure (a) with variable channel geometries: round and droplet-shaped (b) and different orientations during manufacturing: with vertical (XZ) inclinations to the working platform of 22.5° and 45° and different horizontal (XY) orientations of 0°, 40°, 70° and 100° (b). The X and Y directions indicate the build platform and the Z axis shows the build direction. (c) Modified droplet-shaped geometry used in the final test elements.

P_{CL} = 180 W, v_{CL} = 1000 mm/s, E_L = 0.180 J/mm, that provided the smallest possible roughness.

2.2. Roughness analysis using confocal laser scanning microscopy

The roughness measurements of the outer surfaces were carried out according to the standard EN ISO 25178 [48] using the confocal laser scanning microscope ZEISS LSM 700 (Zeiss AG, Oberkochen, Germany), which enabled imaging of larger surfaces at the high magnification by using the workstation PILine and the stitching picture function of the imaging software ZEN 2012 (black edition; Zeiss AG, Oberkochen, Germany).

Similar areas of ~2.44 × 2.44 mm² were investigated for all samples using stitched 2 × 2 image combinations recorded at 50 × magnification. The scanning step size in the Z direction was 3 µm. The scan speed was nine frames per second with a scan resolution of 2.5 µm/pixel. The images were quantified using the software ConfoMap (Zeiss AG, Jena, Germany). The 2-dimensional arithmetic mean height S_a was determined from the data following:

$$S_a = \frac{1}{A}\iint_A |Z(x,y)|dxdy \quad (1)$$

The arithmetic mean height S_a corresponds to the distance of each point from an imaginary mean surface Z divided by the entire surface A.

All planar surfaces with different inclination angles were analysed under the same confocal laser scanning microscope conditions and always directly at the geometric centre of the examined face.

2.3. Analysis of internal channels by X-ray computed tomography

CT was carried out for all cylinders manufactured with internal channel structures using a Phoenix Nanotom tomography (phoenix|x-ray Systems + Services GmbH, Wunstorf, Germany) with a source voltage of 230 kV, a current of 160 µA, an exposure time of 1000 ms, an averaging/skip of 3/1 with a 360° rotation. The resulting pixel size was 12 µm. The raw data was converted from the software phoenix_datos|x_2_aquisition via phoenix_datos|x_2_reconstruction (GE Sensing & Inspection Technologies GmbH, Wunstorf, Germany) into stacks of 1600 two-dimensional (2D) slices that were finally analysed as three-dimensional (3D) volumes in the software AVIZO.

The reconstructed channels were evaluated quantitatively: the geometric deviation from the target shape was analysed in 2D on cross sections of the channels (in total 1600 slices per cylinder axis). Firstly, the area A and perimeter P for the 9 channels on each section were measured. Then, the shape characteristics roundness and equivalent diameter were analysed to evaluate the geometric accuracy of the channels. The roundness Φ was calculated as:

$$\Phi = \frac{4\pi \times \mathbf{A}}{\mathbf{P}^2} \quad (2)$$

wherein a roundness of equal to 1 corresponds to an ideal circular shape.

The equivalent diameter D_e relates to the projected circular shape of the corresponding channel surface and was determined as:

$$\mathbf{D_e} = \sqrt{\frac{4 \times \mathbf{A}}{\pi}} \quad (3)$$

Mean values of the equivalent diameters and roundness were computed over the length of the channel from the analyzed sections. An average value obtained from three similar channels provided a high level of statistical verification.

The channel morphology was analysed by means of the local principal curvatures of channel surfaces. For this, the principal radii of curvature r_1 and r_2 of each point on the surface were determined, from which the two principal curvatures, $\kappa_1 = 1/r_1$ and $\kappa_2 = 1/r_2$, were computed. First, a surface of the voxel-based volume was created from the segmented surface using the software AVIZO. The resulting surface is a triangular approximation of the segmented volumes. The curvatures were then calculated considering two direct neighbours to a certain triangle of the surface and the initial curvature values were smoothed by averaging them four times with the curvature values of direct neighbour triangles (more details in our previous work [49]. The local mean curvature H is expressed as:

$$\boldsymbol{H} = \frac{\kappa_1 + \kappa_2}{2} \quad (4)$$

2.4. CT analysis of final test segments

All demonstrative elements with internal channels were quantitatively analysed using 3D computed tomography acquired with the Phoenix Nanotom (phoenix|x-ray Systems + Services GmbH, Wunstorf, Germany) tomograph using similar scanning parame-

ters: a source voltage of 100 kV, a current of 120 μA, an exposure time of 2000 ms, an averaging/skip of 3/1 with a 360° rotation. The resulting pixel size was (7.5 μm)^3. The raw data was converted from the software phoenix_datos|x_2_aquisition via phoenix_datos|x_2_reconstruction (GE Sensing & Inspection Technologies GmbH, Wunstorf, Germany) into stacks of 1200 two-dimensional (2D) slices and analysed three-dimensionally (3D) using the software AVIZO. The 3D reconstructed surfaces were compared with the nominal ones, resulting in an analysis of geometric deviations depending on the radial orientation in the channel. Roundness Φ, equivalent diameter D_e and 3D curvature distribution of the channel surfaces were calculated according to the procedure presented in Section 2.3.

3. Results

3.1. Contour parameter optimization: External flat surfaces

3.1.1. Platform positioning analysis

The positional effect of the sample arrangement on the LPBF working platform for boundary and centre positions on the arithmetic mean roughness S_a is shown in the contour plot diagram of Fig. 4. Six positions, the upper (T: top) and lower (B: bottom) boundary positions at the extreme left (L: left), middle (M: middle), and extreme right (R: right), are compared with a centrally located sample (C), as shown in Fig. 1(**b**)).

All samples were produced with contour parameters of P_{CL} = 180 W, v_{CL} = 1600 mm/s and a resulting line energy of 0.113 J/mm using the chess scan strategy for the volume part. The measured surface was 2.44 × 2.44 mm^2 for all positions and the geometric middle of the sample surfaces were chosen. For all inclinations the mean values of the measurements at three neighbouring points were used.

Deviations of up to 1.5 and 4 μm were found for the 45° upskin and 90° upskin surfaces around the respective averages of S_a of 9.01 ± 0.33 μm (45°) and 11.17 ± 1.44 μm (90°) for all measured points in the boundary positions of the platform. The 135° downskin orientation, in contrast, causes much larger deviations (up to 11.2 μm) and the average value (S_a = 52.80 ± 3.41 μm). As the surface inclination increases, the accumulation of irregularly distributed sintering defects grows, especially for the upper 135° (downskin) ones located directly on the powder layer, which is quantitatively represented for the comparative maximum heights of the S_Z profiles for the 0.64 × 0.64 mm^2 sections in Fig. 5.

The best surface quality was consistently obtained in the lower right corner for all surface orientations. The roughness generally increases slightly in the bottom-top direction for surfaces inclined at 45° and 90° (ΔS_a = 0.1 and 0.5 μm), and more significantly for 135° (3.7 μm). Similarly, the roughness increases from the right to the left side of the build platform. This is most pronounced for the downskin surfaces (up to 3 μm variation), and smallest for upskin regions with a 45° surface normal (0.3 μm; for 90°: up to 1.6 μm).

In order to avoid the influence of the location on the working platform during the optimization of the contour parameters and channel shapes, samples were only produced in the central part of the platform for the next steps.

3.1.2. Contour vector scan sequence

The influence of the scan sequence of volume and contour vectors on the averaged S_a for the upskin (45°), the inskin (90°) and downskin (135°) surfaces for both linear and chess volumetric scan strategies is shown in Fig. 6. All samples were produced with the same initially chosen LPBF contour parameters (E_L = 0.113 J/mm: P_{CL} = 180 W and v_{CL} = 1600 mm/s). An average of three neighbour-

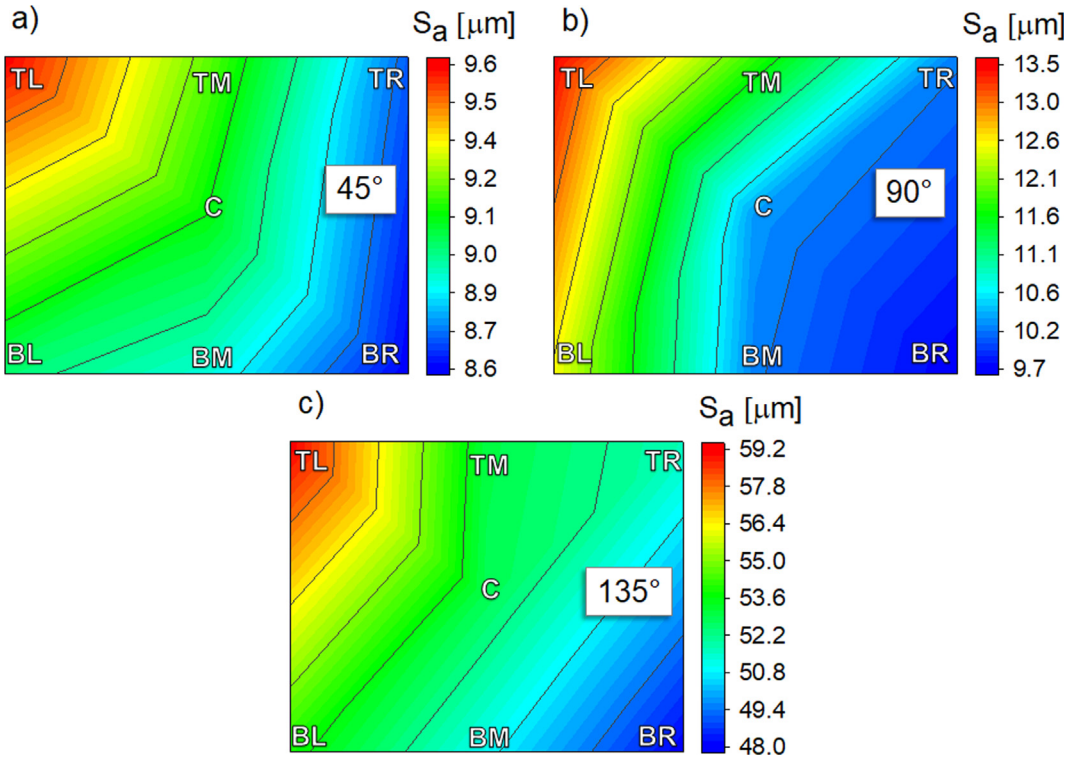

Fig. 4. Effect of the specimen placement on the working platform on the arithmetic mean roughness S_a of flat outer surfaces inclined at 45° (a), 90° (b) and 135° (c) with respect to the build direction (T: top; B: bottom; L: left; M: middle; R: right; see also Fig. 1). All samples were fabricated with contour parameters P_{CL} = 180 W, v_{CL} = 1600, E_L = 0.113 J/mm using the chess scan strategy. The scan sequence inside (bulk) → outside (contour) was used for all samples. Measured areas: 2.44 × 2.44 mm^2. The mean values of the measurements at three neighbouring points were taken.

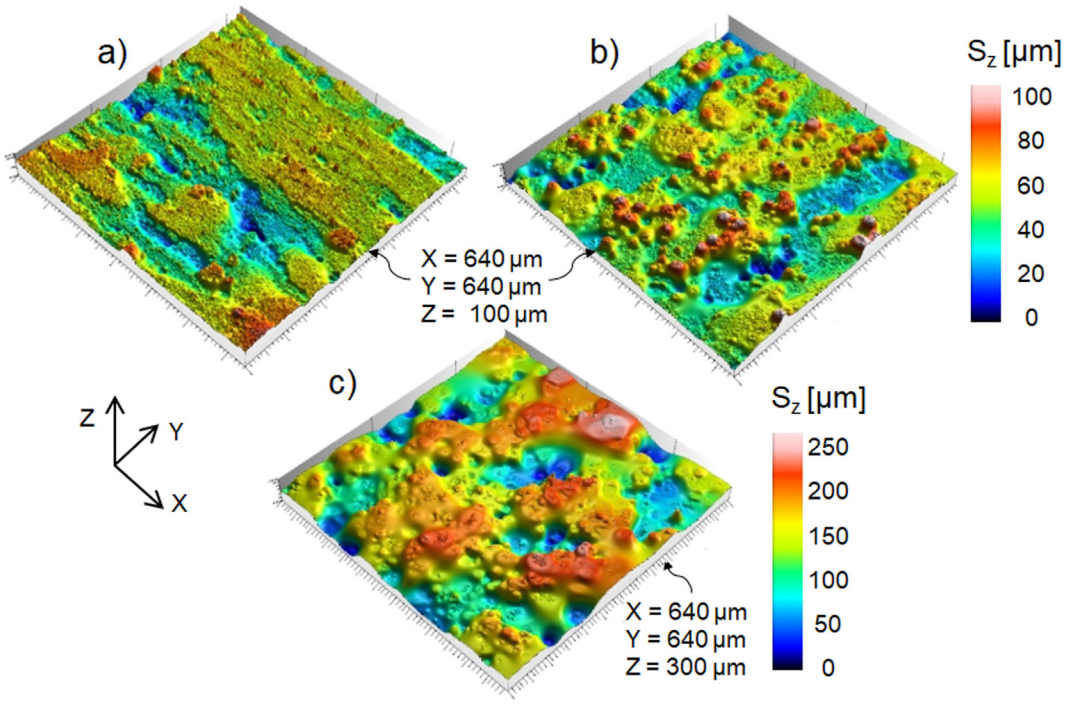

Fig. 5. Typical 3D roughness profiles for (a) 45° (upskin), (b) 90° (inskin) and (c) 135° (downskin) surfaces measured by LSM (area: 0.64 × 0.64 mm^2). All surfaces were manufactured with E_L = 0.113 J/mm, P_{CL} = 180 W and a chess bulk hatching. The inside → outside scan strategy was used. The colour indicates the maximum profile height S_z.

ing measured sections of 2.44 × 2.44 mm^2, located in the geometric centre of the examined surfaces, was computed.

A small effect of the bulk hatching strategy is observed for all variations of contour-bulk scan sequence. Independent of the surface direction as well as the scan sequence, the linear hatching strategy generally shows slightly smaller surface roughnesses compared to chess hatching.

The scan sequence lasering the bulk part first before scanning the contour vectors (i.e. "inside → outside") results in the smoothest surfaces independent of the hatching strategies of the sample bulk: S_a values of 7.4, 10.0, and 57.7 µm are obtained at 45°, 90° and 135° inclinations (linear hatching), respectively. The values obtained with chess hatching are ca. 10% larger in general.

The scanning sequence in Fig. 6 is presented in the order of increasing roughness. Changing the strategy from "inside → outside" to inside followed by double contour scanning, or to more complex scan sequences always terminating with final contour vectors leads to a deterioration of the surface quality independent of the orientation of the surface under consideration.

3.1.3. P_{CL}-v_{CL} variation at a constant line energy density

The influence of a simultaneous variation of the contour laser power P_{CL} and scan speed v_{CL} at a constant energy density E_L of 0.133 J/mm was investigated for the conditions presented in Table 2. The measured sections of 2.44 × 2.44 mm^2 were located in the centre of the analysed surfaces. For all inclinations the mean values of the measurements at three neighbouring points were taken. The arithmetic average height S_a for the upskin (45°), the inskin (90°) and downskin (135°) surfaces for both linear and chess volumetric scan strategies is shown in Fig. 7((a), (b) and (c), respectively), with v_{CL} and P_{CL} represented on the lower and upper axes, correspondingly.

The results show an ambiguous trend in the influence of P_{CL}-v_{CL}: a distinct optimum in S_a is observed for medium v_{CL} values around ~1000–1200 mm/s. This effect is inherent in all inclined surfaces, both for linear and chess bulk hatching strategies.

Thus, for example, for a vertical (inskin, 90°) surface Fig. 7 (b)), the arithmetic mean roughness S_a sharply decreases from 13.2 µm to 8.7 µm with an increase in scan speed v_{CL} from 600 mm/s to 1000 mm/s for the linear and from 17.3 µm to 9.6 µm for the chess bulk hatching strategy, respectively. An increase in scan speed from 1000 mm/s up to ca. 1400 mm/s results in relatively stable S_a with slight deviations from the average of 9.1 ± 0.5 µm and 10 ± 0.6 µm (chess/linear strategies, respectively), thus providing a minimum in S_a. A subsequent increase of v_{CL} to 1800 mm/s leads to a sharp jump in (Fig. 7 (b)) S_a to 11.7 and 12.8 µm for linear and chess hatching. Similar trends were observed for the 45° and 135° surfaces.

The linear strategy again potentially provides somewhat smoother surfaces in all the variations studied. However, the chess hatching strategy is usually recommended, e.g., to reduce the effect of residual stresses [28,29]. Minimizing residual stresses is an important final factor in LPBF fabrication of complex components such as advanced combustion chambers. Therefore, only the chess hatching strategy is considered for the subsequent fabrication of specimens with internal channels.

3.1.4. Contour energy density variation

The line energy density E_L introduced into the contour region was varied in a series of samples by means of changing the scan speed v_{CL}. P_{CL} = 180 W was kept in order to retain comparability with previous results. The varied v_{CL}, and, consequently, the associated E_L values are presented in Table 2. Areas of 2.44 × 2.44 mm^2 were analysed and average value computed from measurements in the three neighbouring regions.

The average S_a of the samples in this series for the upskin (45°), the inskin (90°) and downskin (135°) surfaces (Fig. 8) establishes once again a roughness optimum for medium scan speeds around 1000 to 1200 mm/s. Clearly, the contour energy density can be linked to this distinct optimum for all inclined surfaces, with the minimum region corresponding to an E_L around 0.180 J/mm. Increasing E_L from 0.086 J/mm to 0.18 J/mm caused a significant

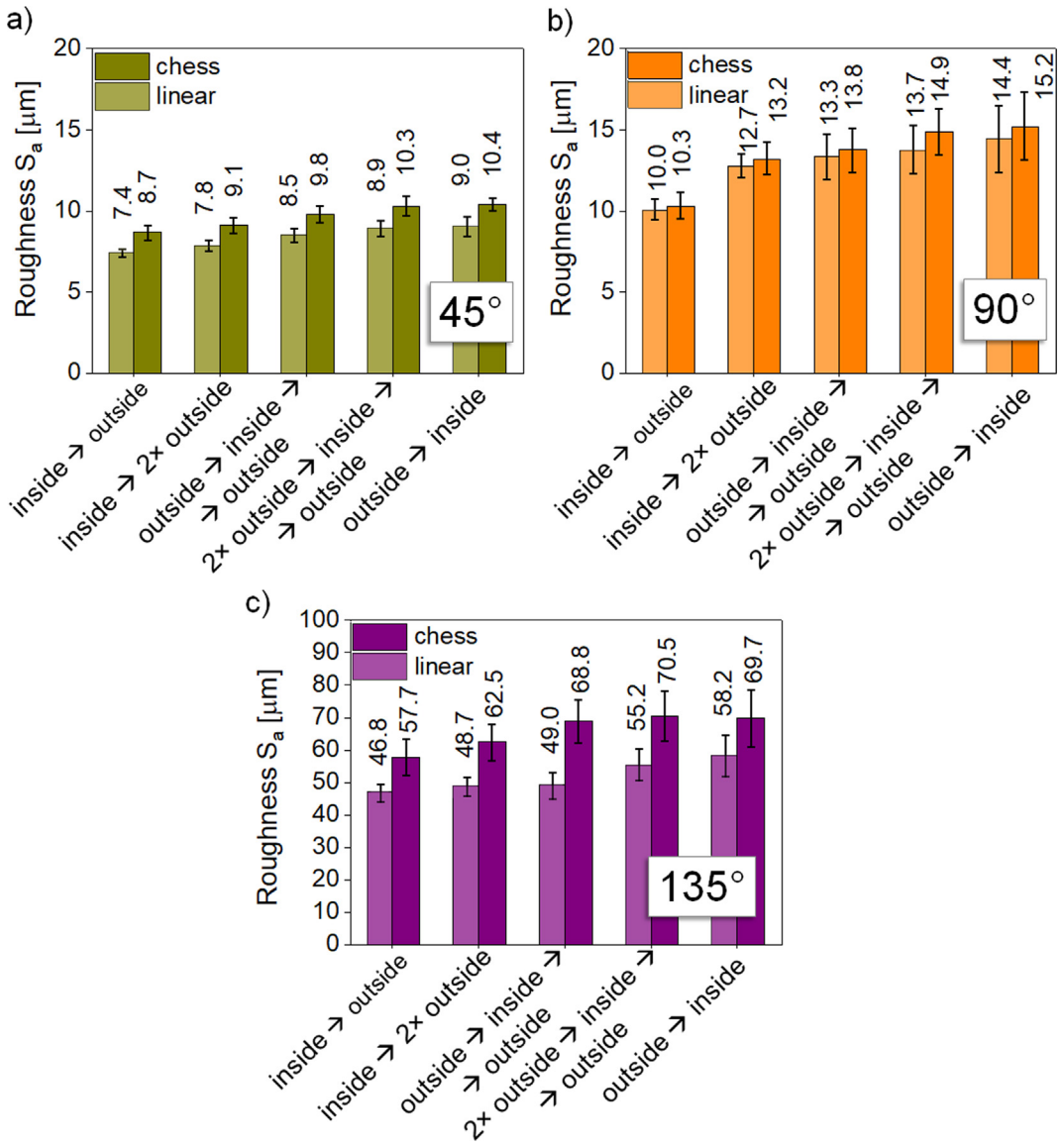

Fig. 6. Influence of the laser scan sequence of the volume and contour vectors in LPBF fabrication for the: (a) vertical inskin (90°), (b) upskin (45°) and (c) downskin (135°) surfaces. All samples were produced with the same initially chosen LPBF contour parameters (E_L = 0.113 J/mm, P_{CL} = 180 W, v_{CL} = 1600 mm/s). Chess and linear indicate the hatching strategies used for the sample bulk. Average values of measurements in three neighbouring regions of 2.44 × 2.44 mm^2 in the centre of all sample surface are presented.

decrease in roughness: the averaged S_a values reduce dramatically from 12.5, 14.9 and 80.5 µm to 6.8, 7.2 and 47.5 µm for the inclination of 45°, 90° and 135° (green, orange, and violet bars in Fig. 8, respectively). A further increase in E_L from 0.18 to 0.3 J/mm leads to higher S_a of 7.5, 8.5 and 56.7 µm at 0.225 J/mm and 8.5 µm at 0.3 J/mm.

For comparison, the left-hand side of the diagram in Fig. 8 shows the average surface roughness values of the specimens made without contouring, which are significantly higher than those for the optimum contouring energy of 0.18 J/mm.

3.1.5. Selection of optimal contour parameters for the final test elements (Section 2.1.3)

Based on the results of the contour parameter optimizations, a set of parameters consisting of P_{CL} = 180 W and v_{CL} = 1000 mm/s at a resulting linear energy density of E_L = 0.180 J/mm is chosen. The inside → outside scan strategy (fusion of the bulk before the outer contours) was selected as optimal strategy and used for the manufacturing of the final test elements in the third part of our study to optimize the wall segments with internal channels.

In order to minimize the influence of the sample positioning on the analysis of the final test elements, all specimens were produced in the central part of the working platform.

3.2. Build direction effects on internal shaped surfaces

Simultaneous to the optimization of contour parameters on outer surfaces (Section 3.1), the influence of different build directions on the surface quality, shape, and continuity of internal shaped surfaces was studied using the set of initially chosen parameters (P_{CL} = 180 W, v_{CL} = 1600, E_L = 0.113 J/mm chess hatching, inside → outside scan sequence). The cylinders included three sets of channels with target diameters of 500, 700 and 1000 µm and were manufactured in the directions of 0°, 22.5°, 45° and 90° with respect to the working platform (see Fig. 2 and **Fig. S2).**

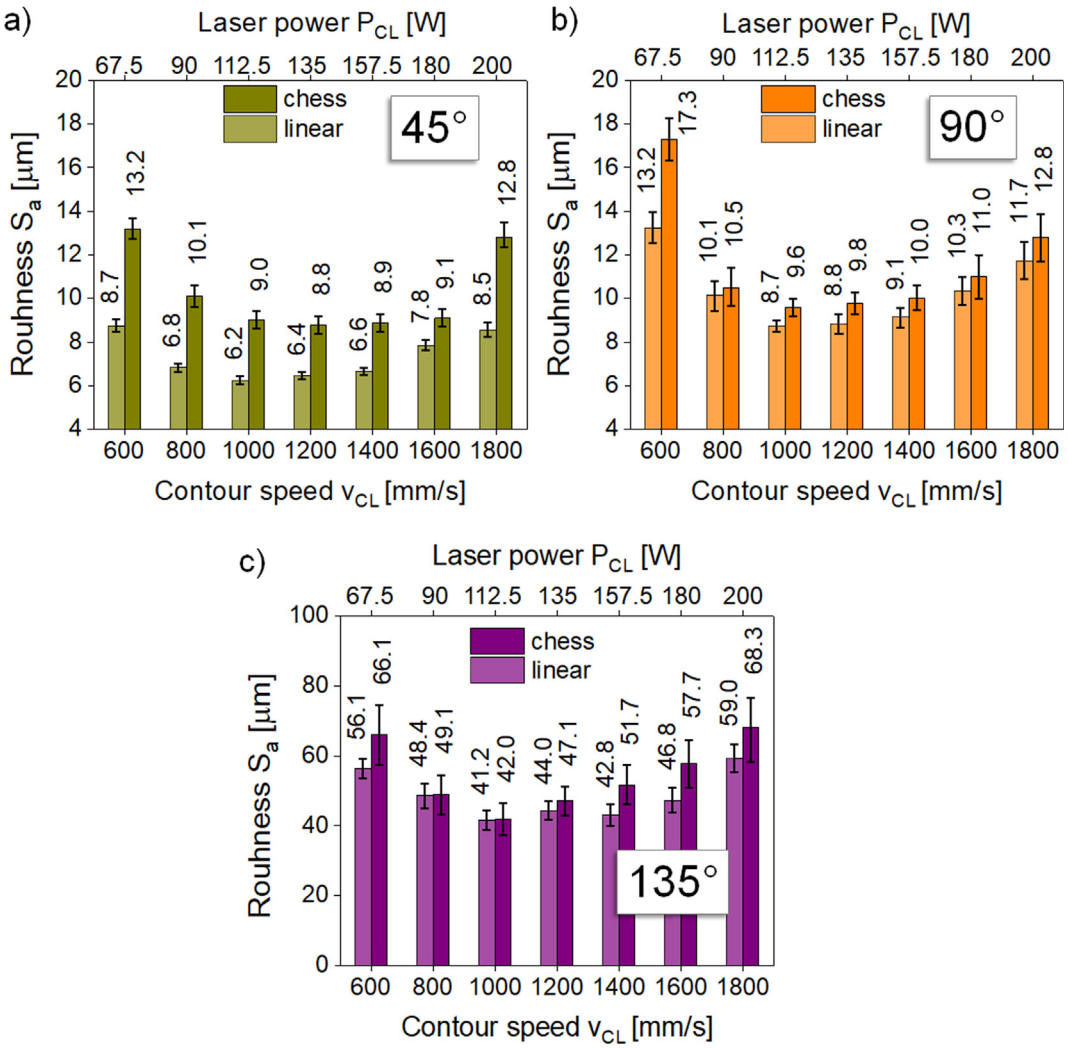

Fig. 7. Simultaneous P_{CL}-v_{CL} variation at constant E_L = 0.113 J/mm: (a) for upskin (45°) (b) for vertical inskin (90°), and (c) for downskin (135°) surfaces. "Chess" and "linear" indicate the bulk hatching strategies. The laser scan sequence "inside → outside" was used for all samples. All analyzed surfaces are 2.44 × 2.44 mm^2. An average of three measurements at neighbouring points were taken.

The channel quality changes dramatically with the orientation: from a flattened and hard-to-pass form with a multitude of adhering powder particles and melt beads at 0° (Fig. 9 (a)), the channels become devoid of obstructions when oriented at 90° (Fig. 9 (d)).

The convex surfaces (H ~ 0.03 μm^{-1}, red colour) of attached particles prevail on the upper surfaces of cylinders at 0° and 22.5°, reduce significantly at 45° and almost completely disappear in vertical channels of 90°.Consequently, the equivalent diameter is reduced sizably to D_e = 805 ± 26 µm and the roundness does not exceed Φ = 0.37 ± 0.12 for channels lying flat at 0° (Fig. 9 (a)). Obviously, in a horizontal position even at diameter of 1000 µm presents a challenge. However, D_e increases significantly at higher inclinations from D_e = 820 ± 22 µm and 952 ± 14 µm for the 22.5° (Fig. 9 (b) and 45° (Fig. 9 (c)), respectively, to 988 ± 10 µm for the vertical 90° specimen (Fig. 9 (d)). The roundness of the channel increases also significantly from Φ = 0.37 ± 0.12 and reaches 0.96 ± 0.02 for the vertical build direction (90°), which is closest to an ideal round shape.

The CT results show that channels in build directions below 45° require a modification of the shape in the raw CAD model in order to achieve higher circularity after LPBF. The fabricated at 0° and 22.5° orientation droplet-shaped channels are shown in Fig. 10 ((a) and (b), respectively). Visually, these channels have fewer obstructions and their shape descriptors are significantly better: the roundness increases to Φ = 0.57 ± 0.10 and 0.62 ± 0.05 (Fig. 10 (a – b)) compared to the round forms. The equivalent diameter in turn reaches D_e = 910 ± 26 µm and 999 ± 23 µm (Fig. 10 (a – b)), respectively.

It should also be noted that the given droplet geometry has an equivalent diameter D_e and a roundness Φ different from that given for round shapes (as quantified in **Table S1**, **supplementary materials**), but the desired result with the modified geometry aims at a final round shape with a roundness close to ideal, i.e. Φ = 1.

Comparative 3D images of all 9 channels of target diameters of 1000 µm, 700 µm and 500 µm in the samples build at the slopes of 0° and 22.5° (**supplementary materials**, **Fig. S4**) reveal that the quality of the channels is particularly poor at small diameters. Discontinuities detected in CT (marked with dashed black ellipses in **Fig. S4** (a – c)) suggest that melt beads or residual powder even blocked several of these paths. The channels produced at a slope of 22.5° or below are significantly closer to the target shape when using the droplet shape and can ensure better permeability.

The overall results of the influence of build orientation on the production accuracy of shaped channels is summarized by the example of channels with a target diameter of 1000 µm in Fig. 11. Both the averaged roundness Φ and the equivalent diame-

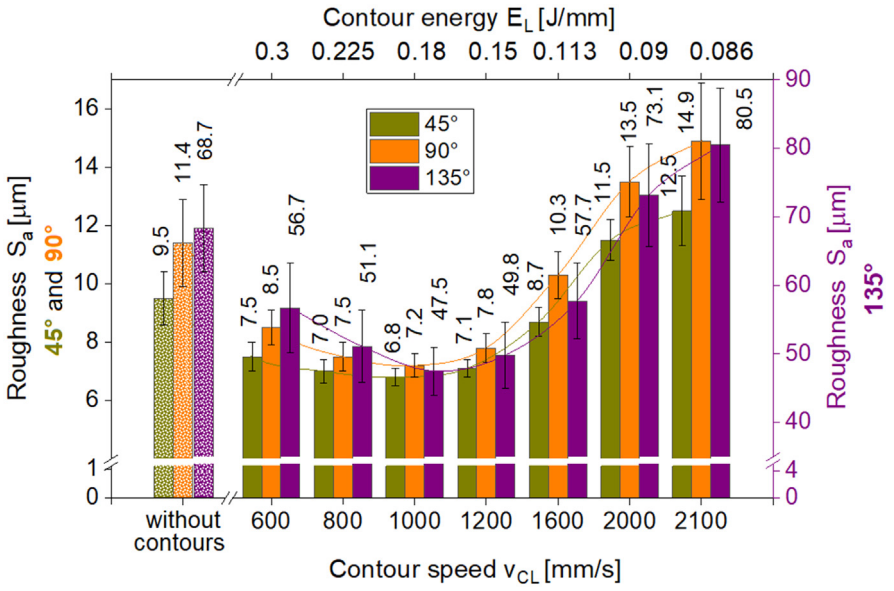

Fig. 8. Influence the contour scan speed (lower x-axis) and line energy density E_L (upper x-axis) at constant P_{CL} = 180 W on S_a for 45° and 90° (both left scale) and 135° (right scale) surfaces (values only shown for bulk chess hatching and the inside → outside sequence). The roughness S_a obtained from specimen produced without using contours are represented on the left. Average values of measurements in three neighbouring points in the geometrically central part of all surface are used.

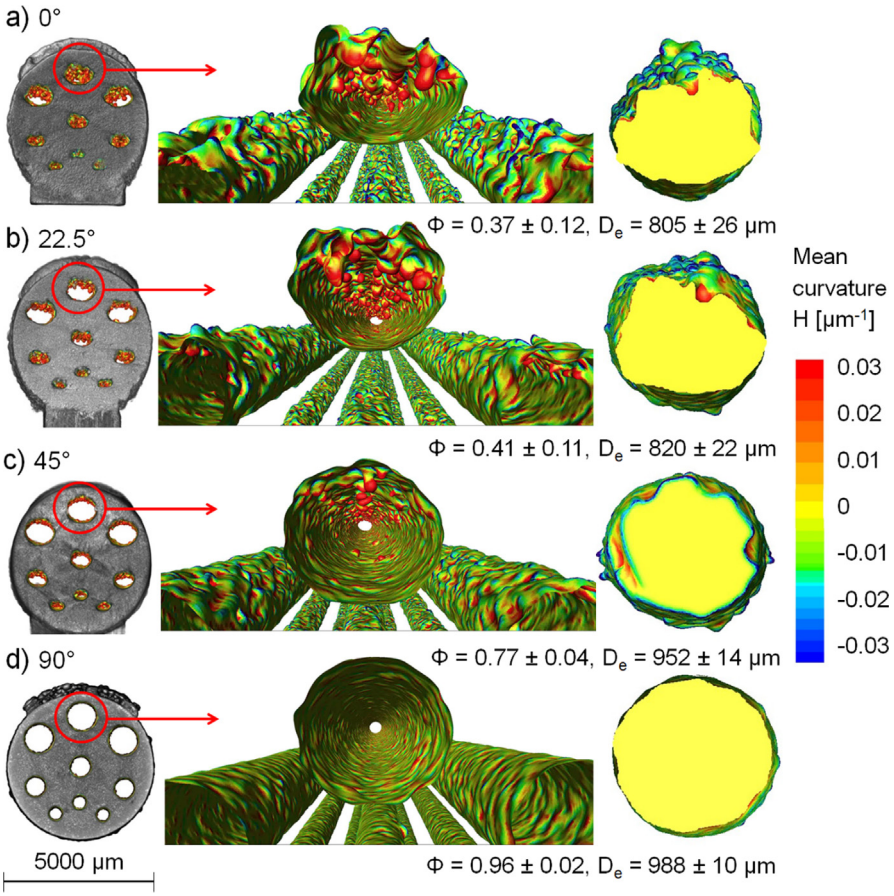

Fig. 9. CT visualization of cylinder with the round-shaped channels produced at the slopes of 0° (a), 22.5° (b), 45° (c) and 90° (d). Left: 3D orthogonal views; middle: isometric 3D views of the selected upper channel with a target diameter of 1000 µm; right: cross sections. Φ: calculated roundness and D_e: equivalent diameter, both averaged over the channel length of all three channels with identical diameter at each orientation. The colour indicates the local mean curvature H (scale on the right).

ters D_e underline again that at higher inclinations the deviations target properties are matched better. For channels with the inclinations of 0° and 45°, the advantage of droplet-shaped channels compared to round ones is obvious. Similar tendencies for the influence of the build direction were also found for the target diameters of 700 µm and 500 µm (**supplementary materials**, **Fig. S5**). However,

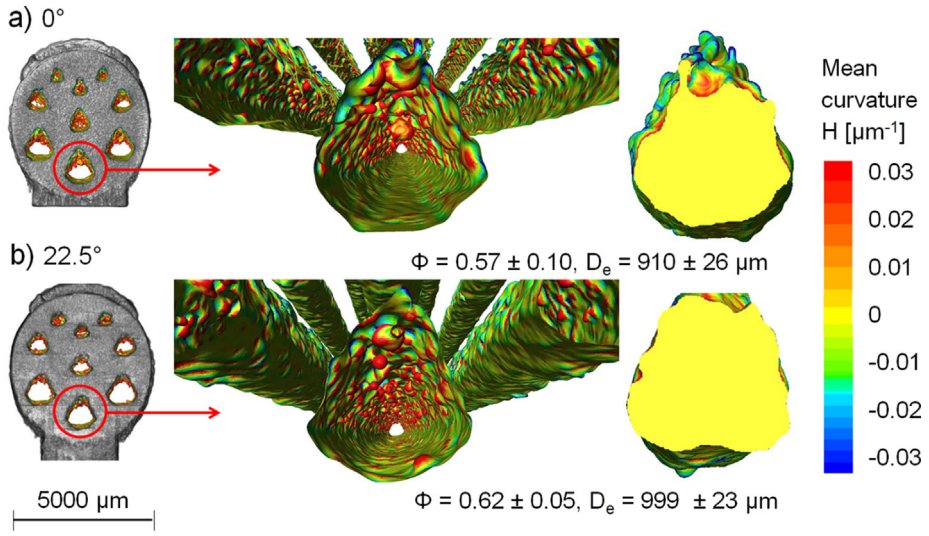

Fig. 10. CT visualization of cylinder with the droplet-shaped channels produced at the slopes of 0° (a), 22.5° (b). The nominal droplet-shaped geometry is shown in Fig. 2**(c)**. Left: 3D orthogonal views; middle: isometric 3D views of the selected upper channel with a target diameter of 1000 µm; right: cross sections. Φ: calculated roundness and D_e: equivalent diameter, both averaged over the channel length of all three channels with identical diameter at each orientation. The colour indicates the local mean curvature H (scale on the right).

when considering fully horizontal channels, a target diameter above 500 µm should be chosen since even droplet-shaped channels turned out to be unreliable in terms of obstruction at the smallest dimension.

3.3. Channel optimization

In the last step, the droplet-shape was further optimized based on the results of the cylindrical samples. The improved droplet-shaped channel geometry was then combined the optimized contour parameters (Section 3.1) and validated using small segments derived from generic combustion chamber cooling geometries.

The build direction effect in the cylindrical samples (Section 3.2) revealed a sharp decrease in the ratio of the channel diameter D_o to its actual height h depending on the inclination. Moreover, the sharp tip shape of the original apex was unfavourable (see, e.g., the triangular shape of the obtained channels in cylindrical samples in Fig. 10 (a -c)). For the vertical channel with a nominal diameter of 1000 µm shown in Fig. 9 (d), for example, the h/D_o ratio was approximately 1, but this ratio decreased due to the channel distinctly flattening at lower inclinations (see **Fig. S2** from (a) to (d) in **supplementary materials**). This loss in height is approximately proportional to the cosine of the inclination: ~0 at 90° (cos (90°) = 0) and ~0.5 at 0° (cos (0°) = 0.5). Taking advantage of this observation, the triangular apex of the original droplet shape was replaced by a smaller circle (**Fig. S3**, **supplementary materials**). The size and distance of this smaller circle from the main channel axis is proportional to the cosine of the inclination. The second circle, scaled with cos(α), was connected by tangential lines with the main circle of diameter D_o. Detailed geometric parameters of the modified droplet-shaped channels, depending on the angle of inclination α, are shown in **Fig. S3** (c) and in **Table S1** in **supplementary materials**).

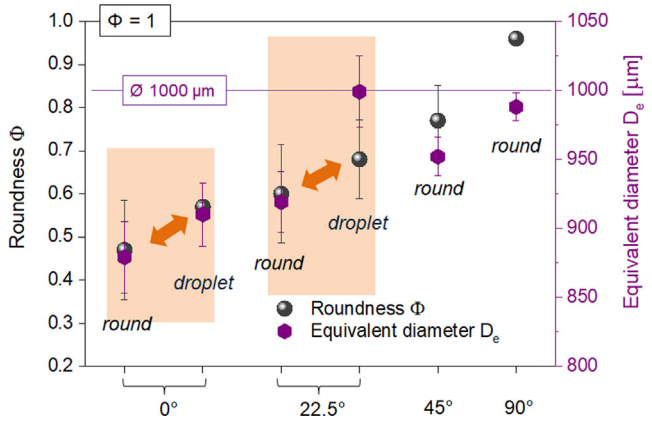

Fig. 11. Build direction effect on the roundness Φ (left y-axis) and equivalent diameter D_e (right y-axis) for the shaped internal surfaces inclined at 0°, 22.5°, 45° and 90° with respect to the working platform. The target diameter of 1000 µm is marked by a violet line. The desired shape for all for is perfectly round, i.e. Φ = 1. Averages of 3 channels along their full lengths are presented. The samples were produced with the machine's initial contour parameters (E_L = 0.113 J/mm). (For interpretation of the references to colour in this figure legend, the reader is referred to the web version of this article.)

The new optimized droplet-shaped channels were compared to round channels also present in every test element. Only the target diameter of 1000 µm was investigated. All contours were produced with the optimized linear energy density of E_L = 0.18 J/mm (P_{CL} = 180 W, v_{CL} = 1000 mm/s, chess hatching, inside → outside scan strategy).

As shown in Section 3.2, the most accurate channel geometry is obtained when the channels are produced vertically (90°) in relation to the working platform (Fig. 11). However, the complex geometry of gas turbine parts, and in particular combustion chambers and other considerations, as for instance support needs or residual stresses in build strategy development may prevent using an optimal orientation for internal channels. Based on the actual geometry of a modern combustion chamber with multidirectional channels orientation, inclinations of 22.5° and 45° relative to the working platform for the LPBF production were chosen.

In order to verify the contour parameter optimisation (Section 3.1), several test elements were also manufactured with the initial contour parameters (E_L = 0.113 J/mm), so that the channels of these finite elements coincide with those in cylindrical samples (Section 3.2, Fig. 10) except for the modified droplet-shaped channels. All coupons were manufactured at four different orientations relative to their own axis, i.e. in horizontal XY orientations of 10°, 40°, 70° and 100° with respect to the recoater direction.

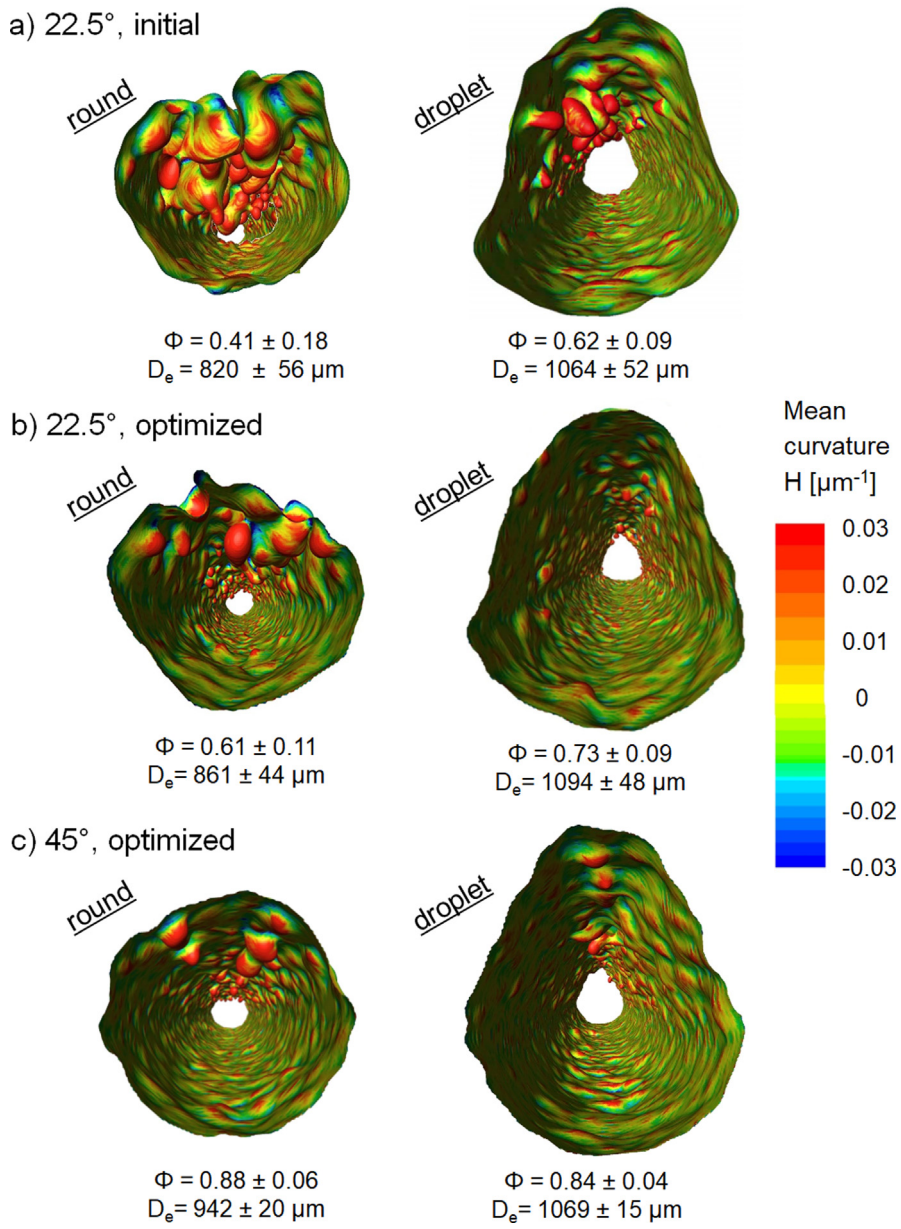

Fig. 12. 3D isometric views of the round and modified droplet-shaped channels (target diameter: 1000 µm) produced with the initial contour parameters (E_L = 0.113 J/mm) at an inclination of 22.5° (a) and the optimized contour parameters (E_L = 0.18 J/mm) at 22.5° (b) and at 45° (c). Φ: roughness and D_e: equivalent diameters, both averaged over the channel length. The colour scale on the right indicates the calculated mean surface curvature distribution H. The specimens were manufactured in the XY orientation of 40°.

The comparison of the round- and modified droplet-shaped channels represented by 3D isometric CT images in Fig. 12 for channels produced at inclinations of 22.5° (a, b - initial and optimized contours, respectively) and of 45°(c; optimized) and a horizontal orientation XY of 40° show sizably different amounts of balling and surface roughness. Particularly the round channels (Fig. 12, on the left) exhibit again a large number of defects with diameters of up to 200 µm adhering to those top surfaces since the melt tracks are unsupported over the powder bed. They are easily identifiable due to their red coloring from the curvature distribution, which indicates a convex local shape relative to the channel walls.

The number of such beads is significantly reduced when (i) optimized instead of initial contour parameters are used (Fig. 12 (a) versus (b)) and (ii) by modifying the channel geometry from round- to droplet-shaped (Fig. 12 (a), left) versus Fig. 12 (a), right)). Naturally, also by increasing the inclination from 22.5° to 45° (Fig. 12 (b) versus (c)) the quality of the inner surfaces improves.

In particular the redesigned droplet geometry leads to an additional improvement in channel quality, as can be seen by comparing the quantitative characteristics of both forms: the primary in the cylindrical samples (Section 3.2) in Fig. 10 (b)) and the modified in the final elements Fig. 12 (b) for the non-optimized contours at 22.5°. Optimized droplet-shaped channels at 22.5° and 45° are almost free of fusion beads. Although attached defects remain present for the round form at the channel inclination of 45°, however, a calculated roundness Φ ~ 0.9 suggests that their number and size are greatly reduced in contrast to the corresponding channels produced at 22.5° (Φ ~ 0.6).

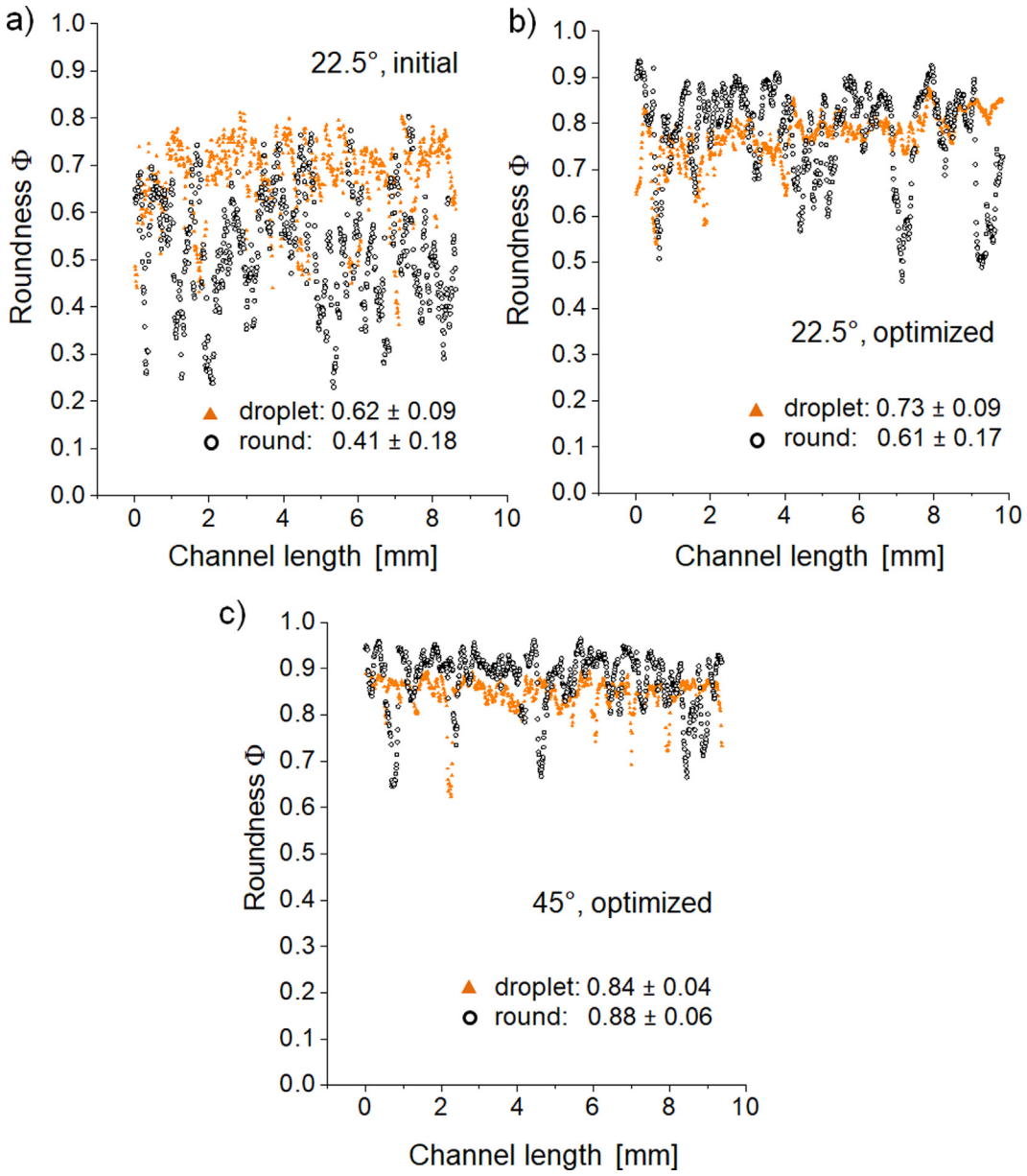

Fig. 13. Roundness Φ of channels in test segments manufactured at of 22.5° with the initial contour parameters (a) and at inclination of 22.5° and 45° with optimized contour parameters (b) (c). Data from samples produced with a horizontal orientation of XY = 40° are presented.

The large roughness of the inner surfaces drastically impairs the basic characteristics of the channels, especially at small inclinations. Variations in roundness Φ along the 10 mm channel length for all types of channels are presented in Fig. 13**,** where (a) shows channels produced with initial contour parameters at 22.5°, and (b) and (c) channels with optimized ones, respectively. The roundness values also exhibit a generally large scattering at the low inclination, whereas at an inclination of 45° less scatter and values close to ~0.9 resulted. Optimized droplet-shaped channels at 22.5° and 45° are almost free of fusion beads. They are present for the round form at 45°, however, a calculated roundness of ~0.9 suggests that their number and size are greatly reduced in contrast to those produced at 22.5° and with a roundness of ~0.6.

The roundness Φ for the different XY directions are shown as grouped data points in Fig. 15. At large only small differences in mean values and their deviations are observed. Thus, no significant influence of the orientation of the sample itself on the surface quality was found.

The equivalent diameters D_e for all types of optimized channels and for the two inclinations of 22.5° and 45° were compared in case of samples oriented horizontally in XY = 40°. The deviations from the mean D_e do not exceed 50 μm for 22.5° (Fig. 15 (a)). The values for the droplet shape are closest to the desired target diameter of 1000 μm: 1094 ± 48 μm (roundness: ~0.73), while the originally round channels measure only 861 ± 44 μm. The effective diameters for 45° are 942 ± 20 μm and 1069 ± 20 μm for the round and droplet shapes, respectively (Fig. 15 (b)).

Thus, neither a modification of the channel geometries in the CAD model nor the contour parameters alone is sufficient to achieve sufficient channel qualities. The best manufacturing results are obtained when the modified channel shapes are combined with properly optimized parameters (Fig. 12**,** Fig. 13**,** Fig. 14**).** In that case, even the relatively flat oriented channels at

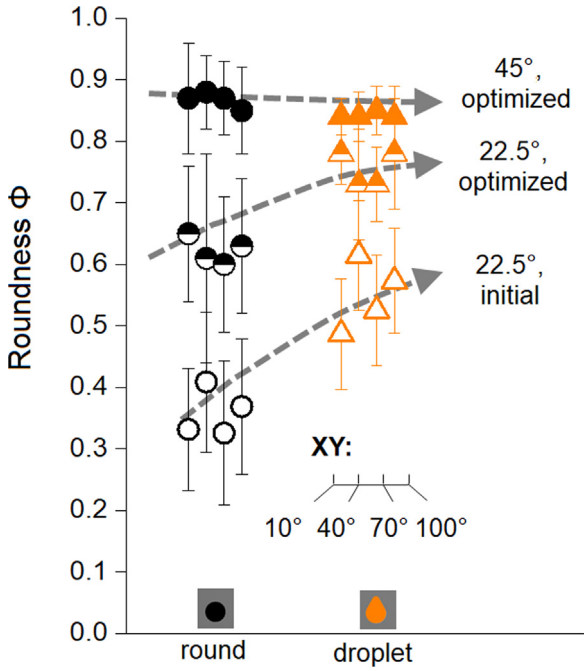

Fig. 14. Roundness Φ averaged over 10 mm channel length for the round and droplet shape of channels produced with initial and optimized contour parameters at build directions of 22.5° and with optimized at 45°. The same samples had a different orientation on the working platform (XY = 10°, 40°, 70° and 100°, as illustrated in Fig. 3 (b)).

22.5° are obtained with smooth, high geometrical accurate surface and the deteriorating downskin defects are strongly reduced.

4. Discussion

4.1. The role of platform positioning for surface roughness

First of all, effects arising from the positioning on the working platform on the quality of the outer surfaces were analysed. While platform positioning effects on bulk material properties related to heterogeneous gas flow in the build chamber have been considered previously (e.g., defect formation [28,37,51] or increased oxidation [52]), their role for surface properties has received much less attention.

When examining samples at the extreme and the centre positions, relatively small deviations of S_a were observed for the upskin and inskin surfaces, while the downskin regions showed increased variability and overall rather poor, almost five times larger S_a values (Fig. 4). The origin of the variations due to sample placement appears to be related to the Argon flow, the flow direction of which (from right to left, see Fig. 1) coincides with the general roughness increase observed in all cases. The Argon flow, for instance, transports away fumes that negatively affect beam quality. The right lower part of the working platform shows the best results in terms of surface quality, even slightly lower than its central part. On the left side, farthest from the argon source, and, particularly in the upper left corner, only poor surface qualities are obtained, showing that part placement on the build platform has to be considered when analysing the contour properties.

Placing all further specimen for channel investigations in the centre of the platform, the influence of positioning was minimized.

4.2. Contour parameter and scan strategy effects on the roughness of the external flat surfaces

The variation of LPBF contour parameters such as scan speed, laser power, and the scan strategy allowed a minimization of the arithmetic mean roughness S_a of flat external surfaces inclined at the angles of 45°, 90° and 135° with respect to the working platform (Section 3.1).

The importance of the contour parameters for external roughness has been discussed in many works, but the systematic optimization approach for the contour parameters chosen here, "laser power - scan speed" and "scan speed - energy density", has not yet been reported for the surface manufacturing of parts produced by LPBF.

Only a few efforts have been carried out to improve the contour properties of Inconel 718 LPBF parts through the variation of contour power and scan speed, for example, Gockel et al. [38] who used this approach. In the latter study, vertical inskin surfaces showed a decrease in S_a at higher laser power (S_a ~ 15, 12, 9 μm

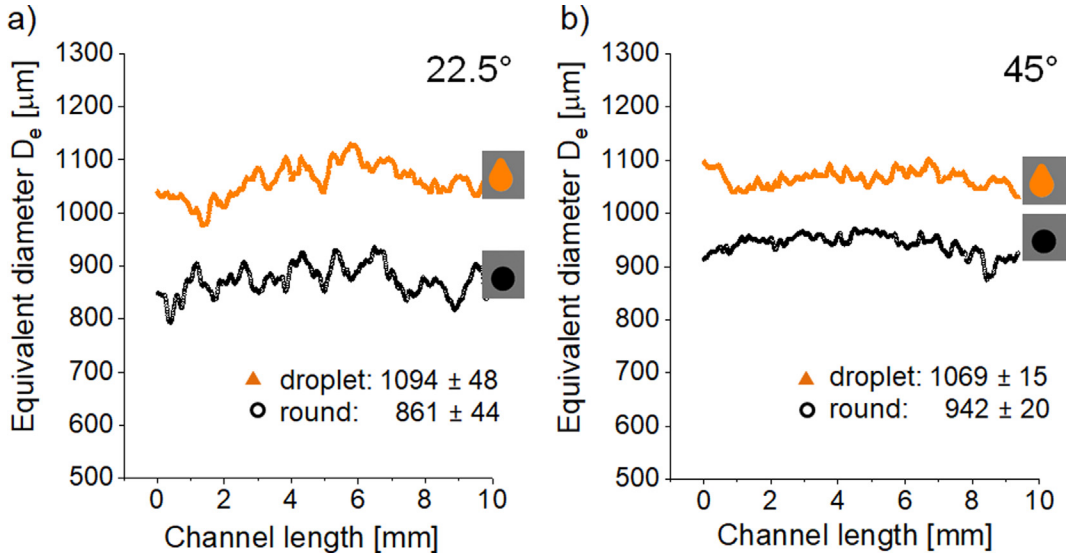

Fig. 15. Equivalent diameters D_e averaged over the 10 mm length for all types of channels manufactured with optimized contour parameters for the inclinations of 22.5° (a) and 45° (b). Data from channels with manufactured with a horizontal orientation of XY = 40° are presented.

at P_{CL} = 80, 100, 120 W at a constant scan speed of 560 mm/s, respectively), providing very similar surface qualities to those obtained here. However, the inverse scan velocity variation did not show a clear trend (S_a remained at ~15 μm for v_{CL} values between 560 and 850 mm/s at P_{CL} = 80 W). Gockel and co-workers argued that an increase of melt pool size at higher laser powers reduces the surface roughness [38]. While this argument at first look also appears to be valid for decreasing scan velocities, the trend shown in Fig. 8 providing a minimum in S_a suggests that this argument cannot explain the increase observed for small v_{Cl}. A thorough determination of melt track sizes as a function of contour parameters and local geometry will be required to investigate this correlation further.

The impact of the laser vector sequence between volumetric part or contours were investigated with an initial parameter set of P_{CL} = 180 W and v_{CL} = 1600 mm/s, resulting in an E_L of 0.113 J/mm, and different scan sequences. The "inside → outside" strategy showed the overall best results for both linear and chess hatching strategies of the bulk part, providing a $S_a \approx 10$ μm for e.g. for the 90° inskin sides (Fig. 6 (b)). This scanning order was used in further optimisation in Sections 3.1.2 and 3.1.4.

The inverted "outside → inside" strategy, in turn, leads to partial remelting of the already solidified outer contour region, leading to the worst S_a values of all scan sequences analysed (e.g., $S_a \approx$ 15 μm for 90°). This is even much higher than S_a of samples produced merely with bulk vectors and no contours (Fig. 8; e.g., $S_a \approx$ 10 μm for 90°; note that S_a was substantially reduced to 6.8 μm when using the optimized parameters with E_L = 0.18 J/mm, v_{CL} = 1000 mm/s, P_{CL} = 180 W). This observation can be understood since scan vectors ending near (or at) a surface is known to lead to a more inhomogeneous surface compared to vectors that parallel the outer contour [55]. Ending melt tracks have been reported to strongly affect surface roughness and particle attachment, and a correlation between hatch distances and arithmetic mean roughness was established [27]. Even if advanced scanning techniques such as "sky-writing" are used to connect to neighbouring vectors, this effect is present to a reduced degree [27]. However, "sky-writing" was not implemented in the employed Concept M2 machine.

In fact, this explanation is also consistent with the result that a chess hatching strategy generally resulted in slightly enlarged S_a values (typically ~10% higher) as compared to linear hatching: In case of the linear scan strategy the sample orientation resulted in scan vectors largely parallel the sample border that at an angle of ~15° in every 2nd layer (90° turns between layers). In contrast, in the chess pattern all vectors are rotated by ~30° (and ~75°) with respect to the sample borders (45° to the platform axes). In between chess islands, the scan direction changes by 90°, and in between layers a 45° turn and lateral shift was applied to the patterns in the current study. Therefore, the chess patterns practically always result in ending or beginning scan vectors near the sample border in every layer, whereas in a linear hatching pattern oriented only at a slight angle to the sample border fewer melt tracks terminate at the surface. In every 2nd layer, the outermost hatching vectors may even act as contour line for the present and the layers beneath, thus leading to an improved surface quality.

The variation of the line energy density E_L by changing scan speeds at the fixed power led to a distinct optimum for all surfaces with an averaged roughness of S_a = 6.8, 7.2, 47.5 μm at E_L = 0.18 J/mm for the upskin (45°), inskin (90°) and downskin (135°) surfaces, respectively (Fig. 8). Compared to the inskin and upskin surfaces, however, the downskin surfaces always show high roughness values, which is inherent to the LPBF process and provoked by the location above the powder bed (causing inward melting into the powder) and local heat accumulation [27,53] and others]. The effect of significantly increased roughness of the downskin surfaces has been noted in several studies, (e.g. [16,19,20,48,54]), although the focus was not on a detailed quantitative analysis in those cases.

While measurable for all surface normal orientations, particularly apparent in the present results was the more sizable effect of the bulk hatching patterns onto the outer surface qualities of downskin borders (Fig. 5). Again, the S_a values were consistently larger for chess hatching patterns compared to the linear scan strategy, which we also can tentatively link to the increase in the melt track size occurring at the vectors endings as inferred from coaxial melt pool imaging [55]. The increase of the melt pool size in a downskin region may, see below, consequently result in a stronger local inward melting into the powder bed beneath the specimen.

The optimized contour parameters were used in the third stage of this work for the final optimization of the inner inclined mini-channels.

4.3. Build direction effect on the internal channels: Roundness and diameters

The effect of the build direction on the quality of internal channels was investigated in two stages. First, the orientation effects were studied as function of the vertical inclination on channels of 500, 700 and 1000 μm diameter by x-ray CT using cylindrical samples (Section 3.2) with standard contour parameters.

Since tactile or optical standard methods for measuring the roughness of the outer surfaces cannot be used for characterisation of curved internal surfaces, the most promising approach is non-destructive X-ray computed tomography (CT) and has been used for the current analysis. CT has already been used to examine internal canals of different configurations, e.g. [15–18], but the approaches for analysis and comparison differ widely. Snyder et al. [17], for example, used the maximum cylindrical concentricity and maximum cylindrical run-out for analysis. A geometric comparison between a scanned object and a CAD file is typically available in most post-processing software and can be also used for geometric quality analysis [56]. However, when using CT metrology in a systematic channel optimization, the low spatial resolution and error sources such as scattering effects present obstacles [43].

The comprehensive analysis of equivalent diameters D_e, roundness Φ and radial deviations in the present study yields an overview of the surface properties along with quantitative estimates of texture characteristics as a function of channel geometry, build orientation and contour parameters. The channels with the most accurate D_e are obtained in the vertical orientation of 90° (Fig. 9 and Fig. 11), consistent with literature [20–23]. However, in the complex geometries of gas turbine components such as combustion chambers, vertical alignment for multidirectional channels often cannot be ensured, so their optimisation at low build angles is a high priority in LPBF.

With the decrease of the build orientation from vertical (90°) to horizontal (0°), the roundness of the larger, 1000 μm wide channels in the cylindrical samples decreased significantly from $\Phi \approx 0.96$ for the to 0.37 (Fig. 11; Section 3.2). The equivalent diameter D_e reduced from ~990 to ~800 μm for the horizontal build direction and the number of downskin defects rendered the channel only semi-passable. The obtained channels have an extremely inhomogeneous roughness distribution with high values in the overhanging downskin region of the channel, which depends strongly on the angle of inclination. Melt beads, in some cases with sizes of up to 150–200 μm, are clearly visible for all different inclinations for round and droplet-shaped surfaces. Due to the locally high laser energy input into the downskin areas (i.e., heat accumulation or overheating) and their unsupported nature, the liquid melt can

penetrate further into powder below [19–21] and cause the formation of such defects. The downskin effects are, thus, the main reason for the loss in geometric accuracy observed in any of the flat channels.

The quality of the inner downskin surfaces at low inclines of 22.5° and 45° was improved by using an elongated droplet shape with a triangular apex. This resulted in a significant improvement of the roundness (e.g., from 0.37 to 0.57 and from 0.41 to 0.62 at 0° and 22.5° inclinations for the target diameter of 1000 μm, respectively; Fig. 9 (a, b) and Fig. 10 (a, b)). While small round channels of 500 μm target diameter were partly unpassable at the inclination of 22.5° or below, similarly small channels with droplet-shape were fully continuous (**Fig. S4, supplementary materials**).

In the second step (Section 3.3), the droplet shape was optimized and simultaneously combined with contour parameters optimized on the outer flat surfaces (Section 3.1). The channel cross-sections in the cylindrical specimen showed a decrease of the effective height approximately proportional to the cosine of their inclination (**Fig. S2**, **supplementary materials**). The sharp triangular apex of the initial droplet shape was unfavourable. Thus, the droplet geometry was improvement by replacing the triangular apex by a smaller circle scaling with the inclination (**Fig. S3**, **supplementary materials**). Moreover, contour parameters optimized on outer surfaces were used in the final test elements (Section 3.3).

The effect of the switch from initial to optimized parameters illustrated in Fig. 12 (a) and (b) consisted of a strong reduction on the scattering of the roundness and diameters besides generally improving both properties. At a steeper inclination of 45°, on the contrary, both the circular as well as the new droplet shaped channels consistently achieved a high roundness near ~0.9 (Fig. 13, Fig. 14). Only the D_e values improved with the modified cross section (Fig. 15 (b)).

The new channel geometry itself resulted in improved overall roundness and a sizable reduction in the number of fusion beads (Fig. 10 (b) versus Fig. 12 (a); inclination of 22.5°). This can be rationalized from a closer analysis of the channel shape and surface orientations building on an approach used by Klingaa and coworkers, who studied the generally increased roughnesses on downskin surfaces of round channels [18 and 50]. These authors used a method, in which the linear or the surface mean arithmetic roughness R_a or S_a, respectively, was computed from the distance to fitted elliptical surfaces along the channel length and shown as a function of the radial (or polar) angle. This provided a maximum roughness at the downskin position (polar angle β = 180°) for any inclination (α) of the channels [18] consistent with common experience in LPBF.

While it is difficult to compare the results of the different sources quantitatively given different channel diameters, different alloys and different characterization (e.g., the varying resolutions in CT), correlating roughness and geometrical precision with angular properties allows a very instructive analysis for a connection with the LPBF build process. The approach can be furthered by accounting for the build inclination in the calculation of the local surface angles, i.e. determining the angle ξ between build direction and the surface normal locally at each spot of the channel (Fig. 16): ξ = 0° corresponds to a horizontal upskin plane, 90° vertical walls, and 180° to downskin regions. For a circular channel cross section, a steeper inclination generally raises the local angles ξ of the inner surfaces of the lower half and decreases them in the top part, both approaching ξ = 90° when the channel is oriented vertically (α = 90°; Fig. 16 (a)). Thus, the downskin surfaces with normals of |ξ| > 135°, which for horizontal round channels scale linearly with β up to 180° (ξ = β), are gradually diminished at steeper build orientations. Generally, it is accepted that surfaces with downskin angles higher than roughly |ξ| ≈ 135–140° (i.e. smaller than 40–45° when defined inversely) require supports and cause particularly deteriorated surface qualities.

This representation also allows to illustrate the advantage of the optimized droplet shapes in terms of the LPBF build process: Despite similarly low build inclinations α, |ξ| only reaches < ~110° (α = 22.5°) and < ~105° (α = 45°) for the larger part of the channel circumference due to the flat plateaus at channel flanks from |β| = 95° to ca. 155°. This accounts for the improvement of the channel properties as shown in the further discussion. Higher |ξ| values, close to the values of the corresponding round channels, result only at |β| > 155° for the relatively narrow top section (the smaller circle in the channel design).

Firstly, the angular analysis (Fig. 17) allows connecting the geometrical accuracy of the round channels obtained in the wall segments with the polar orientation of the local channel region. This verifies that the loss in geometrical accuracy (e.g., Fig. 14) and roundness (e.g., Fig. 13) primarily occurs in the top region roughly between |β| ≈ 100° and 180° for all non-vertical build orientations below α ≤ 90°. The polar diagram Fig. 17 (b) shows again that the loss in effective channel height scaling with decreasing build direction.

In case of the optimized droplet-cross section, a similar trend is obtained in the downskin region although less pronounced, signi-

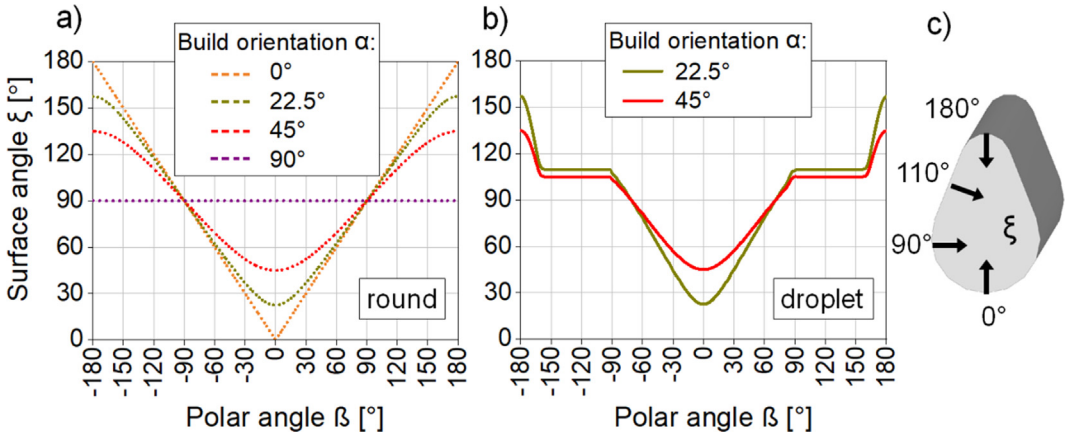

Fig. 16. (a) Change of the angle ξ between build direction and local surface normal of a round channel at different build inclinations of α = 0°, 22.5°, 45° and 90° as a function of polar angle β from the channel axis (β = 0° was defined to be upskin orientation, both the surface normal and build direction are parallel). For α = 90°, only vertical walls ξ = 90°remain. (b) Corresponding surface orientations ξ in the optimized droplet geometry at α = 22.5° and 45°. (c) |ξ| angles for selected regions of the optimized droplet shape shown for an inclination of α = 22.5°.

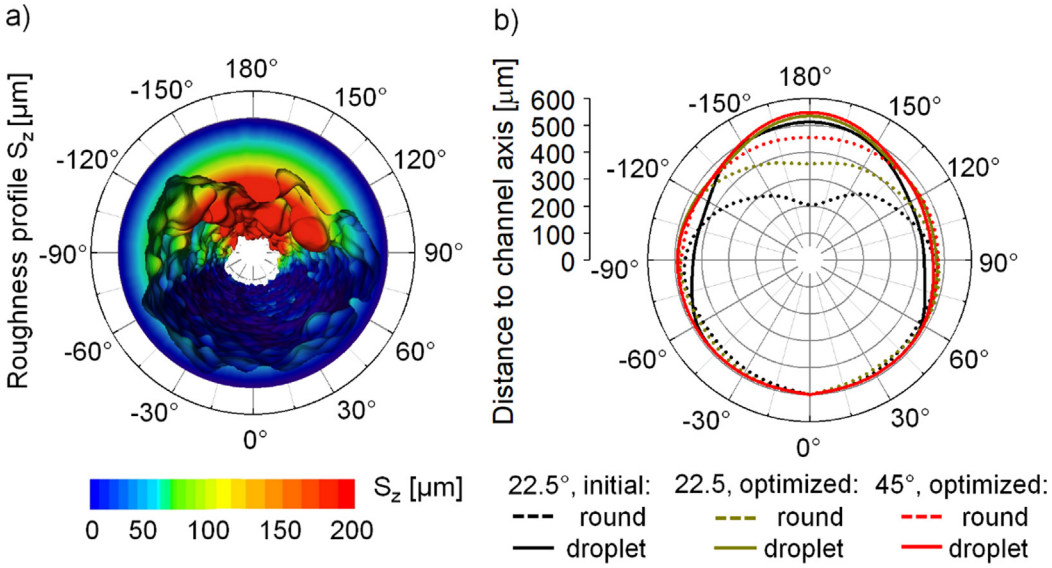

Fig. 17. (a) An example of a 3D deviation profile S_z from the nominal surface of 1000 µm target diameter as a function of polar angle β for the round shape at α = 22.5°. (b) Radial distance profiles from the channel axis averaged over the channel length and smoothed for different channels and build directions α = 22.5° and 45° (round: broken lines; droplet: continuous lines). The data was computed using AVIZO® from the segmented CT data (Section 3.3). A nominal circular channel with a target diameter of 1000 µm corresponds to a radial distance of 500 µm.

fying that the modified shape provides less dependence on the build angle. The channels shape remains larger than the nominal round shape in the long axis of the droplet form. However, the sides of the droplet channels (i.e., up to $|\beta| \leq 150°$) are smaller than the nominal cross section and still vary somewhat for each inclination.

The loss of geometrical accuracy for these channels with relatively small diameters is caused by the poor surface qualities typical and inherent to powder-based LPBF. In order to further understand the usefulness of the modification of the geometries as well as the increase of the build orientations to improve the inner surfaces, R_a was computed from the segmented CT data of the round and droplet-shaped channels of the wall segments (see Fig. 3 and Section 3.3). Given the limited voxel size of $(7.5\ \mu m)^3$ of the CT data, and, thus, an effective resolution of ~22 µm, the R_a values from CT, however, should always be treated with care and can only qualitatively be compared with data from higher resolution methods such the LSM used on the external surfaces. First, the segmented CT data was binarized and then imported as image stack into *python(X,Y)* [57,58]. An elliptical fit carried out with the *numpy* package was applied to each slice for computing the center of gravity. The centers positions of the slides were then fitted with a straight line for subsequent calculations assuming that the ellipse center should ideally remain constant along a straight channel. Next, linear height profiles were computed along the channel length for each distinct radial angle (in 0.1° steps) as a function of the distance *r* to the fitted center of gravity. From these linear height profiles, R_a was computed following Eq. (5):

$$R_{a^-} = \frac{1}{N}\sum_{n=1}^{N}\left|r_n - \bar{r}\right| \tag{5}$$

This approach using R_a profiles along a channel wall instead of S_a (determined form an area) allows computing the roughness in structures with arbitrary cross-sections. The resulting R_a profiles of identical channels (in terms of contour parameters, shape and inclination) in specimen of different XY orientation were averaged and plotted against the polar angle β (Fig. 18 (a)).

The R_a profiles of the 45° inclined channels are generally slightly lower in amplitude than those at the flatter 22.5° build angle. Generally, all profiles are roughly symmetric around the vertical mirror plane (through β = 0° and 180°) of the channel geometry, showing the highest R_a values for high ξangles corresponding to the upper downskin region. Around the bottom center of each channel a slightly increased R_a value (~20 µm for α = 45° and 22.5°) is found, whereas surface angles near 90° corresponding to vertical surfaces lead to a minimum roughness value of ~10–15 µm (these values are, however, close to the voxel size). A similar behavior was observed in Ref. [18] (voxel size $(15.9\ \mu m)^3$) for α = 45° and 30°, which passes into strong local maxima near $|\beta| \approx 45°$ at lower inclinations attributed to the stair case effect [18].

The key feature accounting for the improvement of the channel qualities can be illustrated from the behavior at $90° \leq |\beta| \leq 100°$, where the round and droplet-shaped geometries show qualitative differences: For round shapes at 22.5° inclination, the steep rise of R_a connected with the downskin regions begins at polar angles exceeding roughly $|\beta| \approx 100°$ (R_a up to ~50 µm), i.e. for surfaces bent inwards by ~10–20° from the vertical. For the droplet-shapes, in contrast, the increase is delayed to $|\beta| \geq$ ~150°: The fraction of the channel surface area consisting of critical downskin regions with high surface angles leading to poor quality is strongly reduced by the shape modification (albeit with R_a increasing to ~50 µm at the tip of the droplet cross section, within the limited CT resolution similar to that of the round channels).

The change in behavior of R_a for the different channel regions can also be discerned when the representation of R_a is transformed into a function of the local surface angle ξ with respect to the build direction (Fig. 18 (b)). Depending on the steepness of the inclination, the R_a curves range from 22.5°–157.5° (α = 22.5°) and 45°–135° (45°), showing that the increase in build angle effectively reduces the fraction of downskin area already sizably. In neither case truly horizontal upskin regions (ξ = 0°) remain since the channels are tilted.

Consequently, and connected directly to the shrinking of the range of surface angles at steeper inclines, also the amplitudes of R_a in the channel are reduced from up to ~50 µm (α = 22.5°) to ~35 µm (45°; both shapes). The truncated range of ξ due to

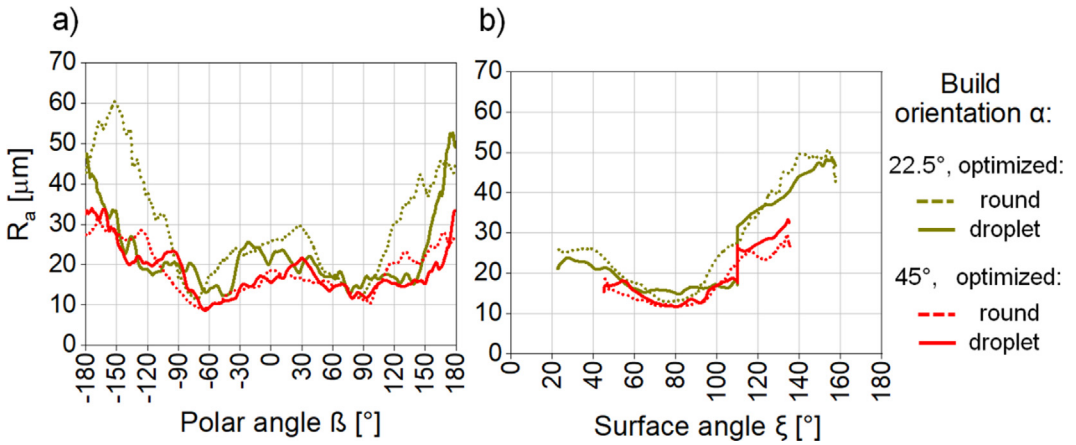

Fig. 18. (a). R_a averaged over the channels of samples at different planer orientations XY for the round and optimized droplet-shaped channels in wall segments produced at inclinations of 22.5° and 45° as a function of polar angle β. (b) Corresponding representation of R_a averaged over both symmetric polar angles ± β of the channel versus the computed angle between the build direction and the surface normal in the nominal CAD geometry at the corresponding polar angle |ξ|. A discontinuity at (|ξ|= ~110°) is observed in this representation for the droplet shapes due to the long linear side sections, which at both inclinations of 22.5° and 45° lead to constant angles of ~110° and ~105° with respect to the build direction.

the steeper build angle almost eliminates the region of extremely poor surfaces (|ξ| ≥ ~135°; corresponding to |β| ≥ ~150° in a horizontal orientation) for the droplet shape: Only an early increase appears to be present. Similarly, for the round shape the angular distribution inside the channel becomes more favorable. Qualitatively, however, the behavior at 45° inclination remains similar, showing a slight minimum of R_a near vertical orientations of |β| = |ξ| = 90° and a subsequent increase for the round and droplet forms at |ξ|≥~110°.

Therefore, the analysis of the roughness as a function of the surface normal angle with respect to the build direction provides a clear link to the LPBF process itself and validates the choice of the scaled droplet design. The analyzed CT data confirm that for the small channels produced in Inconel 718, the optimized shape effectively reduces the fraction of internal surface area to angles of |ξ| ≤ ~135°, reliably eliminating the critical surfaces towards the horizontal top region that is most affected by inward melting and the angular range causing the loss of geometric accuracy. The almost vertical walls with |ξ| = 105° to ~110° that result from the scaled droplet shape design (for ~110° ≤ |β| ≤ ~150°) are more stabilized since they are not primarily over the powder bed.

Thus, minimizing the surface regions with high surface normal orientations |ξ|≥ ~135° by suitable designs is the key in the LPBF manufacturing of these channels.

5. Conclusions

A LPBF strategy was developed for manufacturing internal channels at different build directions in thin-walled in Inconel 718 structures. At the first stage, the LPBF contour parameters were optimized with regard to a minimal roughness of external surfaces with build inclinations of 45°, 90° and 135° with respect to the build platform. The contour scan speed and laser power were varied and the resulting roughness characterized by confocal laser scanning microscopy. The optimal contour parameters P_{CL} = 180 W and v_{CL} = 1000 mm/s (E_L = 0.118 J/mm) with a scan sequence of bulk before contour ("inside → outside") provide a reduction of the arithmetic mean roughness S_a, e.g., to ~7.2 µm for vertical surfaces.

In the second stage, the effect of the build orientation on the quality of internal, free-shaped surfaces were investigated on cylindrical specimens with thin internal channels of 500, 700 and 1000 µm diameter. As the build orientation decreased, inward melting effects of the unsupported, flat downskin regions led to surface defects such as adhering, partially molten residual powder particles or melt beads with a size of up to 200 µm, causing a strong deterioration of the manufacturing accuracy. Notably, for smaller channels the geometric accuracy deteriorated sizably. The use of a droplet-shaped cross section with triangular extension in the downskin section showed sizably increased roundness values and effective diameters closer to the target values.

The results of these investigations allowed an optimization of the channel geometry at inclinations <90° by combining the optimized contour scan parameters with a further optimization of the droplet shape. The triangular extension was replaced by a smaller circle that scales with the cosine of the build orientation, providing extended planar side flanks to the channels. The optimized droplet shape contributed significantly to supressing the formation of the poor downskin sections in the channels and generally improved channel properties:

- at an inclination of 22.5°, the roundness was increased from ~0.4 to ~0.8 (for the droplet-shaped channels with deviations of the equivalent diameter being smaller than 50 µm),
- at an inclination of 45°, a roundness of ~0.9 was obtained for all channel shapes and the target diameter was achieved within 20 µm.

An analysis of the local surface qualities inside the channel as function of the radial position and the build orientation revealed that particularly those surface regions contributed to a loss of geometrical accuracy that reached surface normal angles exceeding ~150° with respect to the build direction. These correspond to particularly flat downskin faces (<30° downskin angle, close to the horizontal) and showed a very high increase of their surface roughness due to melt bead formation from melting into an unsupported powder bed. Thus, it can be confirmed that the modification of the droplet shape using the design scaling with inclination succeeds in effectively reducing the channel area with flat, rather horizontal wall sections at low inclines of 22.5° and 45° as compared to simple round channel cross-sections. This allows for a better stabilization of the melt tracks formed towards the channel top regions. The angular analysis, moreover, provides a data basis for predicting surface roughness as a function of the surface angles in component design.

Therefore, using the optimized contour parameters in conjunction with the modified CAD minimizes these downskin effects and allows manufacturing channels with sufficient roundness and diameters. The presented quantitative results of surface roughness of external and internal structures can be used in further modelling the formation of surfaces in LPBF process simulations.

CRediT authorship contribution statement

Galina Kasperovich: Conceptualization, Investigation, Visualization. **Ralf Becker:** Data Curation. **Katia Artzt:** Validation, Investigation, Software. **Pere Barriobero-Vila:** Primary Reviewing. **Guillermo Requena:** Reviewing and Editing, Project Administration. **Jan Haubrich:** Writing - review & editing, Methodology, Supervision, Project Administration.

Declaration of Competing Interest

The authors declare that they have no known competing financial interests or personal relationships that could have appeared to influence the work reported in this paper.

Acknowledgements

Mr. D. Birlo (DLR Systemhaus Technik, Germany) is gratefully acknowledged for his support in the execution of the LPBF manufacturing processes.

Appendix A. Supplementary material

Supplementary data to this article can be found online at https://doi.org/10.1016/j.matdes.2021.109858.

References

[1] J.P. Kruth, M.C. Leu, T. Nakagawa, Progress in additive manufacturing and rapid prototyping, CIRP Ann: Manuf Techn 47 (1998) 525–540, https://doi.org/10.1016/S0007-8506(07)63240-5.
[2] M. Osakada, Shiomi, Flexible manufacturing of metallic products by selective laser melting of powder, Int. J. Mach. Tool. Manuf. 46 (2006) 1188–1193, https://doi.org/10.1016/j.ijmachtools.2006.01.024.
[3] K.N. Amato, S.M. Gaytan, L.E. Murr, E. Martinez, P.W. Shindo, J. Hernandez, S. Collins, F. Medina, Microstructures and mechanical behavior of Inconel 718 fabricated by selective laser melting, Acta Mater. 60 (5) (2012) 2229–2239, https://doi.org/10.1016/j.actamat.2011.12.032.
[4] B.P. Conner, G.P. Manogharan, A.N. Martof, L.M. Rodomsky, C.M. Rodomsky, D. C. Jordan, J.W. Limperos, Making sense of 3-D printing: Creating a map of additive manufacturing products and services, Additive Manuf. 1–4 (2014) 64–76, https://doi.org/10.1016/j.addma.2014.08.005.
[5] F. Caiazzo, V. Alfieri, G. Corrado, P. Argenio, Laser powder-bed fusion of Inconel 718 to manufacture turbine blades, Int. J. Adv. Manuf. Technol. 93 (2017) 4023–4031, https://doi.org/10.1007/s00170-017-0839-3.
[6] A. Uriondo, M. Esperon-Miguez, S. Perinpanayagam, The present and future of additive manufacturing in the aerospace sector: a review of important aspects, J. Aerospace Eng. 229(11) (2015) 2132–2147, https://doi.org/10.1177/0954410014568797.
[7] C.Y. Yap, C.K. Chua, Z.L. Dong, Z.H. Liu, D.Q. Zhang, L.E. Loh, S.L. Sing, Review of selective laser melting: Materials and applications, Appl. Phys. Rev. 2 (2015), https://doi.org/10.1063/1.4935926 041101.
[8] X. Wang, X. Gong, K. Chou, Review on powder-bed laser additive manufacturing of Inconel 718 parts, Proc. IMechE Part B: J. Eng. Manuf. (2016) 1–14, https://doi.org/10.1177/0954405415619883.
[9] J.R. Davis (Ed.), ASM Specialty Handbook: Nickel, Cobalt, and their Alloys, ASM International, Materials Park, OH, 2000, https://www.asminternational.org/handbooks/-/journal_content/56/10192/06178G/PUBLICATION.
[10] R.C. Reed, The superalloys: fundamentals and applications, Cambridge University Press 31 (07) (2008) 1–392, https://doi.org/10.1017/CBO9780511541285.
[11] W. Gao, Y. Zhang, D. Ramanujan, K. Ramani, Y. Chen, C.B. Williams, C.C.L. Wang, Y.C. Shin, S. Zhang, P.D. Zavattieri, The status, challenges, and future of additive manufacturing in engineering, Computer-Aided Des. 69 (2015) 65–89, https://doi.org/10.1016/j.cad.2015.04.001.
[12] E. Hosseini, V.A. Popovich, A review of mechanical properties of additively manufactured Inconel 718, Addit. Manuf. 30 (2019), https://doi.org/10.1016/j.addma.2019.100877 100877.
[13] T. Vilaro, C. Colin, J.D. Bartout, L. Nazé, M. Sennour, Microstructural and mechanical approaches of the selective laser melting process applied to a nickel-base superalloy, Mat. Sci. & Eng. A 534 (2012) 446–451, https://doi.org/10.1016/j.msea.2011.11.092.
[14] T. Behrendt, T. Richter, A.S. Söhngen, Characterization of Advanced Combustor Cooling Concepts for Metallic and Oxide Ceramic Matrix Composites in a Reacting Flow, in: ASME Turbo Expo 2014, 16. - 20. Juni 2014, Düsseldorf, Deutschland, In: Proceedings of the ASME Turbo Expo: Turbine Technical Conference and Exposition 1A (2014) 26909. https://dx.doi.10.1115/GT2014-26909.
[15] C.K. Stimpson, J.C. Snyder, K.A. Thole, D. Mongillo, Roughness effects on flow and heat transfer for additively manufactured channels, ASME, J. Turbomach. 138 (5) (2015), https://doi.org/10.1115/1.4032167 051008.
[16] C.K. Stimpson, J.C. Snyder, K.A. Thole, D. Mongillo, Scaling roughness effects on pressure loss and heat transfer of additively manufactured channels, ASME J. Turbomach. 139 (2017), https://doi.org/10.1115/1.403455 021003.
[17] J.C. Snyder, C.K. Stimpson, K.A. Thole, D. Mongillo, Build direction effects on additively manufactured channels, J. Turbomach. 138 (2016) 1–8. https://doi.org/10.1115/GT2015-43935.
[18] C.G. Klingaa, T. Dahmen, S. Baier, S. Mohanty, J.H. Hattel, X-ray CT and image analysis methodology for local roughness characterization in cooling channels made by metal additive manufacturing, Addit. Manuf. 32 (2020), https://doi.org/10.1016/j.addma.2019.101032 101032.
[19] A. Charles, A. Elkaseer, L. Thijs, V. Hagenmeyer, S. Scholz, Effect of process parameters on the generated surface roughness of down-facing surfaces in selective laser melting, Appl. Sci. 9 (2019) 1256, https://doi.org/10.3390/app9061256.
[20] J.C. Fox, S.P. Moylan, B.M. Lane, Effect of process parameters on the surface roughness of overhanging structures in laser powder bed fusion additive manufacturing, Procedia CIRP 45 (Suppl. C) (2016) 131–134, https://doi.org/10.1016/j.procir.2016.02.347.
[21] A. Charles, A. Elkaseer, T. Mueller, L. Thijs, M. Torge, V. Hagenmeyer, S. Scholz, A Study of the Factors Influencing Generated Surface Roughness of Downfacing Surfaces in Selective Laser Melting, in: Proceedings of the World Congress on Micro and Nano Manufacturing (WCMNM), Portorož, Slovenia, 18–20 Sept., pp. 327–330. https://doi.org/10.3390/app9061256.
[22] G. Strano, L. Hao, R.M. Everson, K.E. Evans, Surface roughness analysis, modelling and prediction in selective laser melting, J. Mater. Process. Technol. 213 (4) (2013) 589–597, https://doi.org/10.1016/j.jmatprotec.2012.11.011.
[23] P. Das, R. Chandran, R. Samant, S. Anand, Optimum Part Build Orientation in Additive Manufacturing for Minimizing Part Errors and Support Structures, Proc. Manuf. 1 (2015) 343–354, https://doi.org/10.1016/j.promfg.2015.09.041.
[24] M. Langelaar, Combined optimization of part topology, support structure layout and build orientation for additive manufacturing, Struct. Multidiscip. Optimiz. 57 (2018) 1985–2004, https://doi.org/10.1007/s00158-017-1877-z.
[25] A. Triantaphyllou, C.L. Giusca, G.D. Macaulay, F. Roerig, M. Hoebel, R.K. Leach, B. Tomita, K.A. Milne, Surface texture measurement for additive manufacturing, Surf. Topogr.: Metrol. Prop. 3 (2) (2015), https://doi.org/10.1088/2051-672X/3/2/024002 024002.
[26] S. Chowdhury, S. Anand, Part Build Orientation Optimization and Geometry Compensations for Additive Manufacturing Process, J. Manuf. Sci. Eng. 140(3) (2018) 031009 (15 pages), https://doi.org/10.1115/1.4038293.
[27] Y. Tian, D. Tomus, P. Rometsch, X. Wu, Influences of processing parameters on surface roughness of Hastelloy X produced by selective laser melting, Addit. Manuf. 13 (2017) 103–112, https://doi.org/10.1016/j.addma.2016.10.010.
[28] K. Artzt, T. Mishurova, P.P. Bauer, J. Gussone, P. Barriobero-Vila, S. Evsevleev, G. Bruno, G. Requena, J. Haubrich, Pandora's box–influence of contour parameters on roughness and subsurface residual stresses in laser powder bed fusion of Ti-6Al-4V, Materials 13 (2020) 3348, https://doi.org/10.3390/ma13153348.
[29] J.J.P. Kruth, J. Deckers, E. Yasa, R. Wauthlé, Assessing and comparing influencing factors of residual stresses in selective laser melting using a novel analysis method, Proc. Inst. Mech. Eng. Part B J. Eng. Manuf. 226 (2012) 980–999, https://doi.org/10.1177/0954405412437085.
[30] J. Robinson, I. Ashton, P. Fox, E. Jones, C. Sutcliffe, Determination of the effect of scan strategy on residual stress in laser powder bed fusion additive manufacturing, Addit. Manuf. 23 (2018) 13–24, https://doi.org/10.1016/j.addma.2018.07.001.
[31] J.P. Choi, G.H. Shin, S. Yang, D.Y. Yang, J.S. Lee, M. Brochu, J.H. Yu, Densification and microstructural investigation of Inconel 718 parts fabricated by selective laser melting, Powder Technol. 310 (2017) 60–66, https://doi.org/10.1016/j.powtec.2017.01.030.
[32] W.O. Syam, H.A. Al-Shehri, A.M. Al-Ahmari, K.A. Al-Awzzan, M.A. Mannan, Preliminary fabrication of thin-wall structure of Ti6Al4V for dental restoration by electron beam melting, Rapid Prototyp. J. 18 (3) (2012) 230–240, https://doi.org/10.1108/13552541211218180.
[33] M. Jamshidinia, R. Kovacevic, The influence of heat accumulation on the surface roughness in powder-bed additive manufacture, Surf. Topogr.: Metrol. Prop. 3 (1) (2015), https://doi.org/10.1088/2051-672X/3/1/014003 014003.
[34] A. Safdar, H.Z. He, L.Y. Wei, A. Snis, L.E. Chavez de Paz, Effect of process parameters settings and thickness on surface roughness of EBM produced Ti-6Al-4V, Rapid Prototyp. J. 18 (5) (2012) 401–408, https://doi.org/10.1108/13552541211250391.

[35] D. Barba, C. Alabort, Y.T. Tang, M.J. Viscasillas, R.C. Reed, E. Alabort, On the size and orientation effect in additive manufactured Ti-6Al-4V, Mater. Des. 186 (2020), https://doi.org/10.1016/j.matdes.2019.108235 108235.
[36] K.A. Mumtaz, N. Hopkinson, Selective Laser Melting of thin wall parts using pulse shaping, J. Mat. Proc. Techn. 210 (2) (2010) 279–287, https://doi.org/10.1016/j.jmatprotec.2009.09.011.
[37] I. Koutiri, E. Pessard, P. Peyre, O. Amlou, T. de Terris, Influence of SLM process parameters on the surface finish, porosity rate and fatigue behavior of as-built Inconel 625 parts, J. Mat. Proc. Techn., Elsevier, 255 (2018) 536–546. https://doi.org/10.1016/j.jmatprotec.2017.12.043ff.ffhal-01826611.
[38] J. Gockel, L. Sheridan, B. Koerper, B. Whip, The Influence of Additive Manufacturing Processing Parameters on Surface Roughness and Fatigue Life, Int. J. of Fatigue 124 (2019) 380–388, https://doi.org/10.1016/j.ijfatigue.2019.03.025.
[39] B. Whip, L. Sheridan, J. Gockel, The effect of primary processing parameters on surface roughness in laser powder bed additive manufacturing, Int. J. Adv. Manuf. Technol. 103 (2019) 4411–4422, https://doi.org/10.1007/s00170-019-03716-z.
[40] F. Caiazzo, V. Alfieri, G. Casalino, On the Relevance of Volumetric Energy Density in the Investigation of Inconel 718 Laser Powder Bed Fusion, Materials (Basel). 13 (3) (2020) 538, https://doi.org/10.3390/ma13030538.
[41] Z. Baicheng, L. Xiaohua, B. Jiaming, G. Junfeng, W. Pan, S. Chen-nan, N. Muiling, Q. Guojun, W. Jun, Study of selective laser melting (SLM) Inconel 718 part surface improvement by electrochemical polishing, Mat. Des. 116 (2017) 531–537, https://doi.org/10.1016/j.matdes.2016.11.103.
[42] N.N. Kumbhar, A.V. Mulay, Post Processing Methods used to Improve Surface Finish of Products which are Manufactured by Additive Manufacturing Technologies: A Review, J. Inst. Eng. India Ser. C 99 (4) (2018) 481–487, https://doi.org/10.1007/s40032-016-0340-z.
[43] A. Townsend, N. Senin, L. Blunt, R.K. Leach, J.S. Taylor, Surface texture metrology for metal additive manufacturing: a review, Precis. Eng. 46 (2016) 34–47, https://doi.org/10.1016/j.precisioneng.2016.06.001.
[44] J.d.S. Solheid, H.J. Seifert, W. Pfleging, Laser surface modification and polishing of additive manufactured metallic parts, Proc. CIRP 74 (2018) 280–284. https://doi.org/10.1016/j.procir.2018.08.111.
[45] W.J. Sames, F.A. List, S. Pannala, R.R. Dehoff, S.S. Babu, The metallurgy and processing science of metal additive manufacturing, Int. Mater. Rev. (2016) 1–47, https://doi.org/10.1080/09506608.2015.1116649.
[46] A.A. Gomez-Gallegos, F. Mill, A.R. Mount, Surface finish control by electrochemical polishing in stainless steel 316 pipes, Int. J. Manuf. Proc. 23 (2016) 83–89, https://doi.org/10.1016/j.jmapro.2016.05.010.
[47] S.A.E. Aerospace, Aerospace Material Specification: AMS 5662, SAE International, 2009, AMS5662: Nickel Alloy, Corrosion and Heat Resistant, Bars, Forgings, and Rings 52.5Ni 19Cr 3.0Mo 5.1Cb 0.90Ti 0.50Al 18Fe, Consumable Electrode or Vacuum Induction Melted 1775°F (968°C) Solution Heat Treated, Precipitation Hardenable - SAE International.
[48] ISO 25178-2:2012 Geometrical product specifications (GPS) — Surface texture: Areal — Part 2: Terms, definitions and surface texture parameters, 2012, pp. 47, AMS5662M: Nickel Alloy, Corrosion and Heat Resistant, Bars, Forgings, and Rings 52.5Ni 19Cr 3.0Mo 5.1Cb 0.90Ti 0.50Al 18Fe, Consumable Electrode or Vacuum Induction Melted 1775°F (968°C) Solution Heat Treated, Precipitation Hardenable - SAE International.
[49] G. Kasperovich, J. Haubrich, J. Gussone, G. Requena, Correlation between porosity and processing parameters in TiAl6V4 produced by selective laser melting, Mat. Des. 105 (2016) 160–170, https://doi.org/10.1016/j.matdes.2016.05.070.
[50] C.G. Klingaa, M. K. Bjerre, S. Baier, L. De Chiffre, S. Mohanty, J.H. Hattel, Roughness investigation of SLM manufactured conformal cooling channels using X-ray computed tomography, in: 9th Conf. on Industrial Computed Tomography ICT2019, Padova, Italy, 2019. https://core.ac.uk/download/pdf/189891998.pdf.
[51] A. Ladewig, G. Schlicka, M. Fissera, V. Schulzeb, Influence of the shielding gas flow on the removal of process by-products in the selective laser melting process, Addit. Manuf. 10 (2016) 1–9, https://doi.org/10.1016/j.addma.2016.01.004.
[52] C. Pauzon, E. Hryha, P. Forêt, L. Nyborg, Effect of argon and nitrogen atmospheres on the properties of stainless steel 316 L parts produced by laser-powder bed fusion, Mat. Des. 179 (2019), https://doi.org/10.1016/j.matdes.2019.107873 107873.
[53] S. Rott, A. Ladewig, K. Friedberger, J. Casper, M. Full, J.H. Schleifenbaum, Surface roughness in laser powder bed fusion – Interdependency of surface orientation and laser incidence, Addit. Manuf. 36 (2020), https://doi.org/10.1016/j.addma.2020.101437 101437.
[54] S. Patel, A. Rogalsky, M. Vlasea, Towards understanding side-skin surface characteristics in laser powder bed fusion, J. Mat. Res. 35 (15) (2020) 2055–2064, https://doi.org/10.1557/jmr.2020.125.
[55] H. Yeung, B. Lane, J. Fox, F. Kim, J. Heigel, J. Neira, Continuous laser scan strategy for faster build speeds in laser powder bed fusion system, in: Proc. 28th Ann. Int. Solid Freeform Fabrication Symposium – An Addit. Manuf. Conf., 2017. https://www.researchgate.net/publication/321729092.
[56] J.P. Kruth, M. Bartscher, S. Carmignato, R. Schmitt, L. De Chiffre, A. Weckenmann, Computed tomography for dimensional metrology, CIRP Annals 60 (2) (2011) 821–842, https://doi.org/10.1016/j.cirp.2011.05.006.
[57] Python 3.9.5, Python Software Foundation, https://www.python.org/.
[58] Spyder 4.2.1, The Scientfic Python Development EviRonment, https://www.spyder-ide.org/.

Supplementary Materials

The effect of build direction and geometric optimization in laser powder bed fusion of Inconel 718 structures with internal channels

Galina Kasperovich[(a)], Ralf Becker[(b)], Katia Artzt[(a)], Pere Barriobero-Vila[(a)], Guillermo Requena[(a,c)], Jan Haubrich[(a)]

a) Institute of Materials Research, German Aerospace Center (DLR), Linder Hoehe, D-51147 Cologne
b) Institute of Propulsion Technology, German Aerospace Center (DLR), Linder Hoehe, D-51147 Cologne
c) RWTH Aachen University, Metallic Structures and Materials Systems for Aerospace Engineering, D-52062 Aachen, Germany

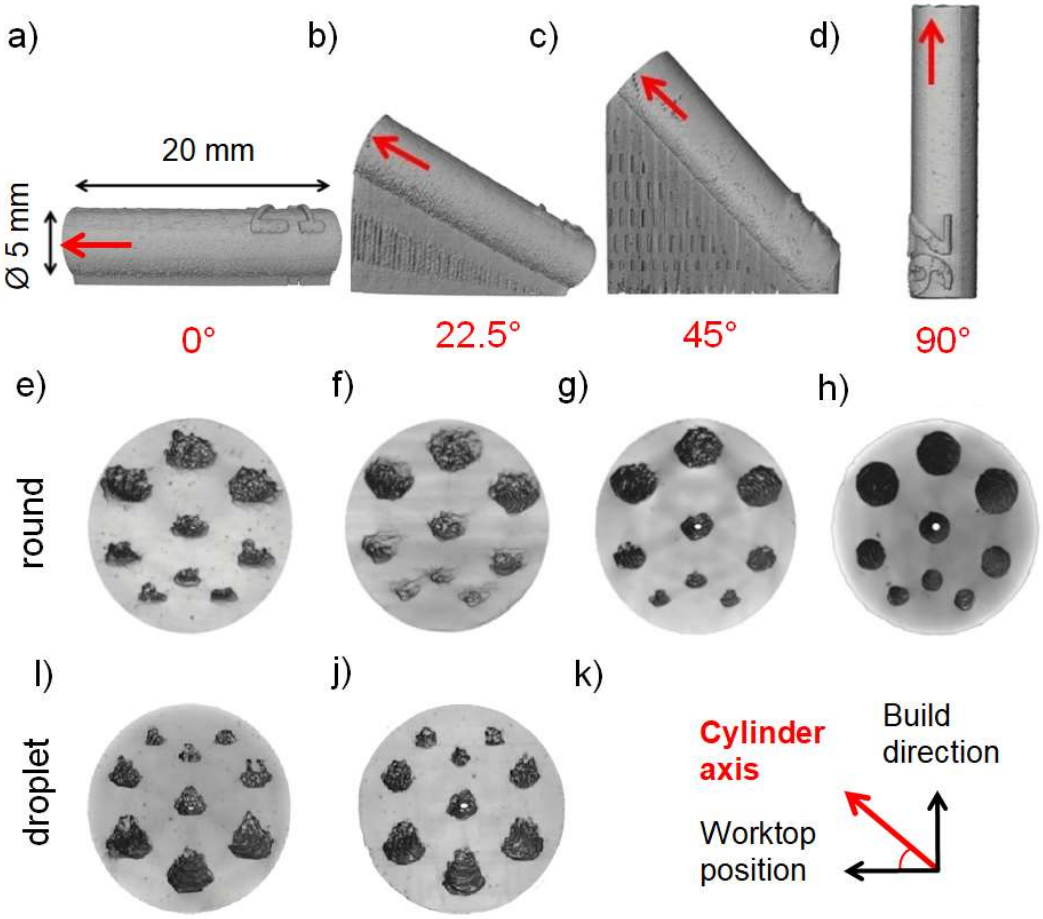

Fig. S1. Side views of cylinders produced with a different slope of the cylinder axis with respect to the working platform: 0° (a), 22.5° (b), 45° (c) and 90° (d). The middle row represents frontal images of cylinders with round channels produced at 0° (e), 22.5° (f), 45° (g) and 90° (h). Below are the cylinders with droplet shaped channels, produced at 0° (i) and 22.5° (j). The target geometry is shown in **Fig. S3** (a, b). The cylinder orientation with in the working platform and build direction corresponds to the scheme (k) and is marked with a red arrow in pictures (a)–(d).

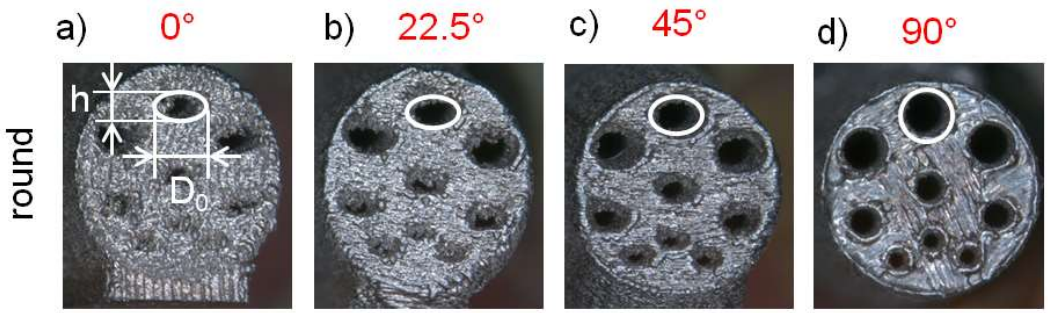

α [°]	h/D_o	$1 - h/D_o$	$\cos(\alpha)/2$
0	0.50	0.50	0.5
22.5	0.55	0.45	0.45
45	0.65	0.35	0.35
90	1.00	0.00	0

Fig. S2. Proposal for adjusting the channel height depending on the inclination angle α: photographic images of channels produced at 0° (a), 22.5° (b), 45° (c) and 90° (d) with the actual profile marked by a white circle for the target diameter D_0 - on the top and approximation of height h using cosine α – in the table below.

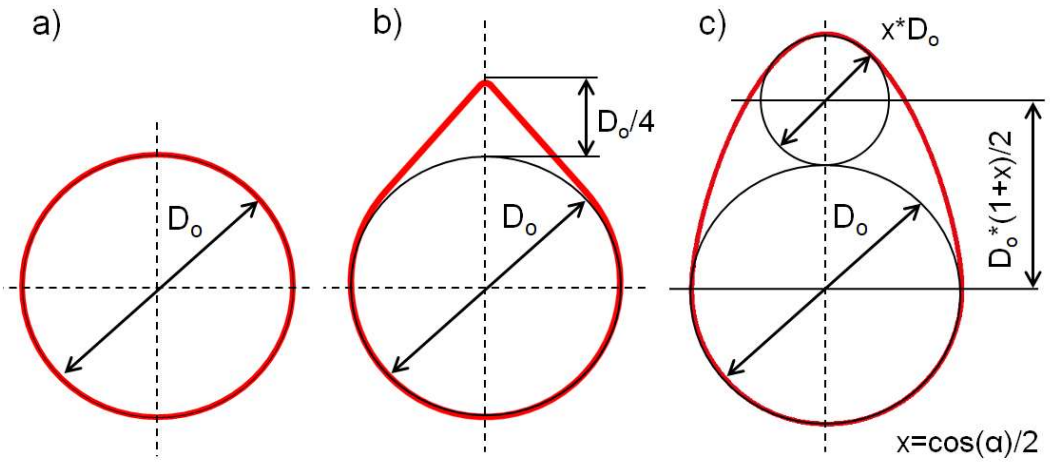

Fig. S3. Round (a) and droplet-shaped channel geometry with a target diameter D_o: (b) - for the cylindrical samples with a sharp-angled peak (Section 2.1.2.) and (c) - an adapted form for the finite test segments (Section 2.1.3.). The numerical parameters are shown in **Table S1**.

Table S1. Numerical parameters of shaped channels as a function of the build direction.

Channel geometry according to **Fig. S3**	Build direc-tion, α [°]	Chan-nels shape	Defined CAD geometry							Target geometry	
			Diameter [µm]		Peak height h [µm]	Area × 10^{-6} [µm²]	Perime-ter [µm]	D_e [µm]	Round ness Φ	D_e [µm]	Round-ness Φ
			base D_0	upper D_u							
b) in cylind-rical samples (Section 2.1.2)	all direc-tions: 0, 22.5, 45, 90	round	500	-	0	0.196	1570	500	1	500	1
			700	-	0	0.385	2198	700	1	700	1
			1000	-	0	0.785	3140	1000	1	1000	1
		droplet	500	-	125	0.214	1709	522	0.920	500	1
			700	-	175	0.419	2393	731	0.919	700	1
			1000	-	250	0.855	3419	1044	0.919	1000	1
c) in final test elements (Section 2.1.3)	22.5	round	1000	-	0	0.785	3140	1000	1	1000	1
		droplet	1000	462	462	1.034	3834	1148	0.883	1000	1
	45	round	1000	-	0	0.785	3140	1000	1	1000	1
		droplet	1000	350	350	0.948	3630	1099	0.904	1000	1
b) Peak height of the droplet channels in the cylindrical samples: $h = D_o/4$											
c) Upper diameter of the droplet channels in the final test segments: $D_u = D_o * \cos(\alpha)/2$											

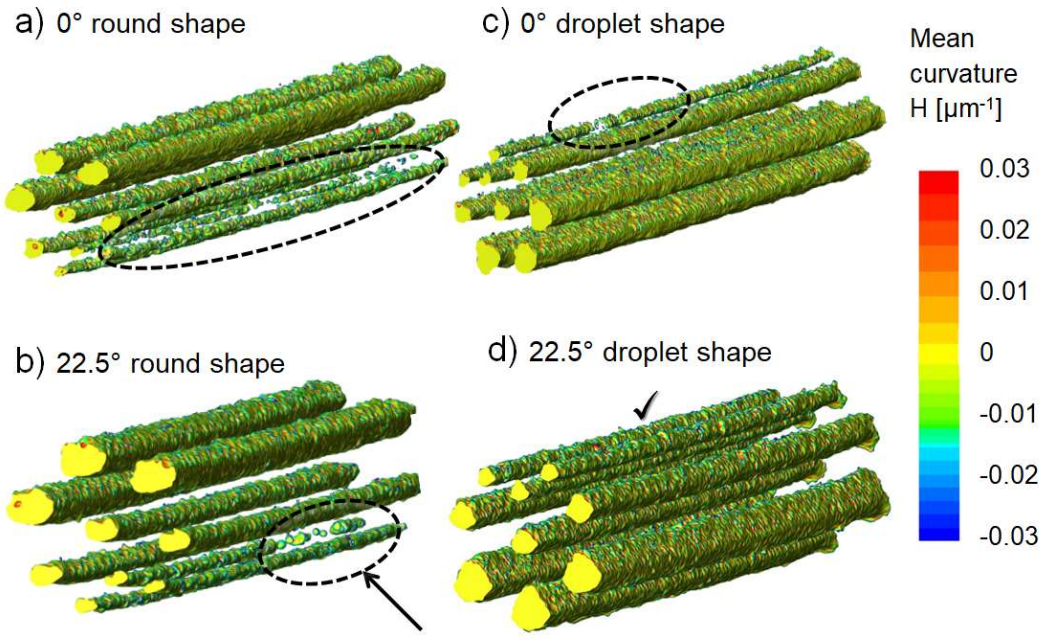

Fig. S4. CT reconstruction of all channels (the target diameters of 1000 µm, 700 µm and 500 µm three times each) in cylinders manufactured horizontally (0°; (a) and (c)) and at an inclination of 22.5°((b) and (d)) to the working platform: round channel shape ((a) and (b)) compared to the droplet form ((c) and (d)). The Inconel 718 material is transparent, and the colour corresponds to

the mean curvature. Discontinuities of small channels are marked by black circles. When using the droplet shape, even the small channels are continuous.

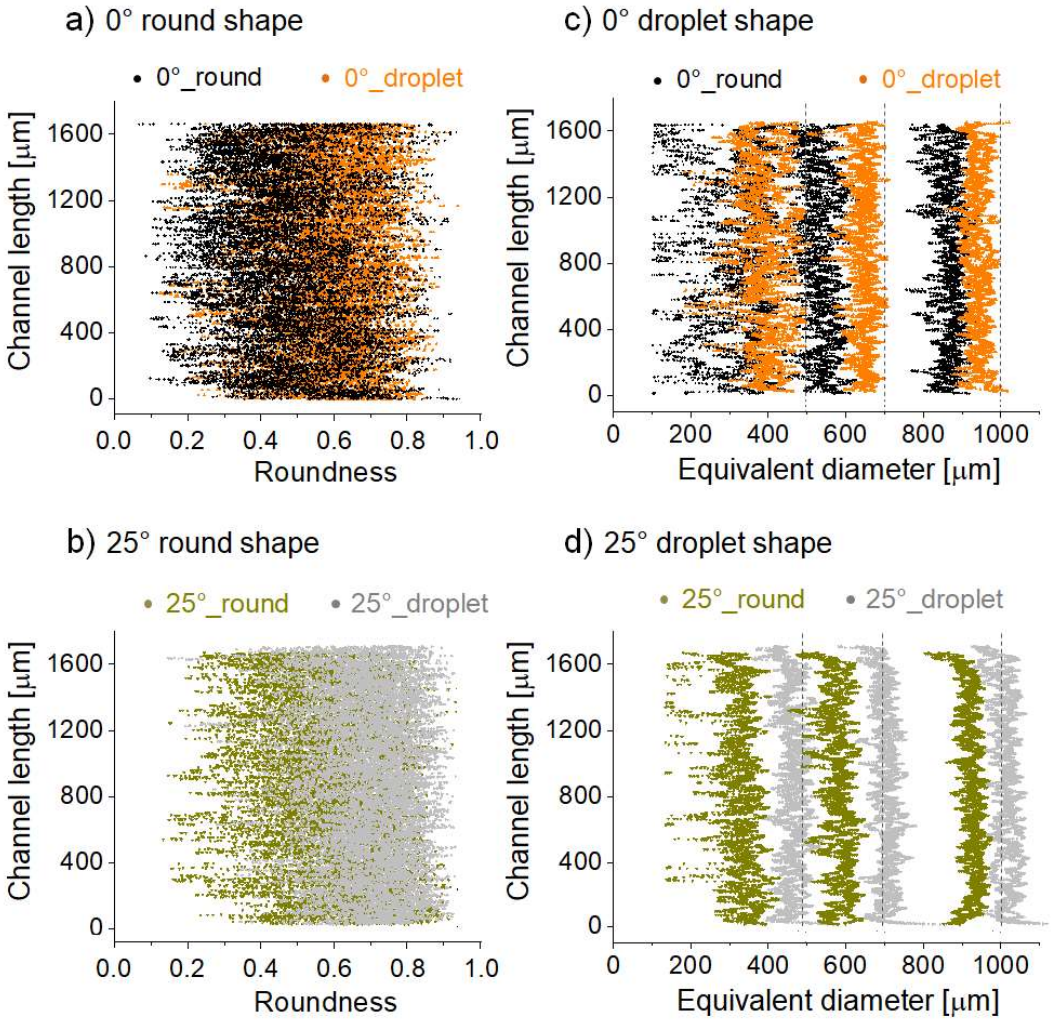

Fig. S5. Roundness Φ (a, b) and equivalent diameter D_e (c, d) of the all channels (3×1000 μm, 3×700 μm and 3×500 μm of the target diameter) at the horizontal manufacturing of 0° (a, c) and inclined at 22.5° (b, d) channels surfaces. The round channel shape (a, b) are compared to the droplet (c, d).